American Mineralogist, Volume 107, pages 2084–2100, 2022

Experimental calibration of an Fe^{3+}/Fe^{2+}-in-amphibole oxybarometer and its application to shallow magmatic processes at Shiveluch Volcano, Kamchatka

Andrea E. Goltz[1,*], Michael J. Krawczynski[1], Molly C. McCanta[2,†], and M. Darby Dyar[3,4]

[1]Department of Earth and Planetary Sciences, Washington University in St. Louis, 1 Brookings Drive, St. Louis, Missouri 63130, U.S.A.
[2]Department of Earth and Planetary Sciences, University of Tennessee at Knoxville, 1621 Cumberland Avenue, Knoxville, Tennessee 37996, U.S.A.
[3]Department of Astronomy, Mount Holyoke College, 50 College Street, South Hadley, Massachusetts 01075, U.S.A.
[4]Planetary Science Institute, 1700 East Fort Lowell, Suite 106, Tucson, Arizona 85719, U.S.A.

Abstract

Oxygen fugacity is an important but difficult parameter to constrain for primitive arc magmas. In this study, the partitioning behavior of Fe^{3+}/Fe^{2+} between amphibole and glass synthesized in piston-cylinder and cold-seal apparatus experiments is developed as an oxybarometer, applicable to magmas ranging from basaltic to dacitic composition. The partitioning of Fe^{2+} is strongly dependent on melt polymerization; the relative compatibility of Fe^{2+} in amphibole decreases with increasing polymerization. The Fe^{2+}/Mg distribution coefficient between amphibole and melt is a relatively constant value across all compositions and is, on average, 0.27. The amphibole oxybarometer is applied to amphibole in mafic enclaves, cumulates, and basaltic tephra erupted from Shiveluch volcano in Kamchatka with measured Fe^{3+}/Fe_{Total}. An average Fe^{3+}/Fe^{2+} amphibole-glass distribution coefficient for basalt is used to convert the Fe^{3+}/Fe_{Total} of amphibole in samples from Shiveluch to magmatic oxygen fugacity relative to NNO. The f_{O_2} of primitive melts at the volcano is approximately NNO+2 and is faithfully recorded in amphibole from an amphibole-rich cumulate and the basaltic tephra. Apparently, higher f_{O_2} recorded by amphibole in mafic enclaves likely results from partial dehydrogenation of amphibole during residence in a shallow andesite storage region. We identify three pulses of mafic magma recharge within two weeks of, a month before, and two to three months before the eruption and find that, at each of these times, the host andesite was recharged by at least two magmas at varying stages of differentiation. Application of the amphibole oxybarometer not only gives insight into magmatic f_{O_2} but also potentially details of shallow magmatic processes.

Keywords: Amphibole, oxybarometer, subduction zones, XAFS, experimental petrology

Introduction

Oxygen fugacity is a key intrinsic parameter for magma genesis. Magmatic oxygen fugacity effects mineral stability, which, in turn, influences magmatic differentiation (e.g., Osborn 1959; Hamilton et al. 1964) and the formation of porphyry deposits worldwide (e.g., Mungall 2002; Core et al. 2006; Richards 2011; Lee et al. 2012; Sun et al. 2013). The oxygen fugacity of primitive magmas is also of interest because it is thought to be reflective of the oxygen fugacity of mantle sources (e.g., Ballhaus et al. 1990; Carmichael 1991; Cottrell and Kelley 2013; Grocke et al. 2016) or pressure, temperature, and degree of melting (e.g., Rowe et al. 2009; Gaetani 2016).

Oxygen fugacity is particularly difficult to estimate for primitive arc magmas. The oxygen fugacity of a melt is most commonly estimated using two-oxide oxybarometry (Buddington and Lindsley 1964), but two-oxide pairs are rare or absent in some natural samples and subject to re-equilibration during cooling (e.g., Hou et al. 2020). Researchers have tried to probe the oxygen fugacity of primitive melts by analyzing olivine-hosted melt inclusions using X-ray absorption near edge structure (XANES; e.g., Kelley and Cottrell 2009; Brounce et al. 2014) and by analyzing their S-speciation (e.g., Rowe et al. 2009). However, because of rapid H diffusion through olivine, the oxygen fugacity determined from a melt inclusion may not reflect the pre-entrapment oxygen fugacity of a primitive melt (Bucholz et al. 2013). Crustal processing such as crustal assimilation and syn-eruptive oxidation may further convolute the oxygen fugacity of primitive melts and make measurements of oxygen fugacity from any of the above methods difficult to interpret as a signature of primitive melt oxygen fugacity (e.g., Mathez 1984; Ague and Brimhall 1988; Lee et al. 2005).

Amphibole is a desirable target for the development of an alternative oxybarometer in arc systems. It is a hydrous mineral commonly found as a phenocryst in andesite, dacite, and rhyolite melts and less commonly in hydrous basalts (e.g., Martin 2007; references therein). It is also a common mineral in cumulates found at arc settings and in suprasubduction zone ophiolites (e.g., Arculus and Wills 1980; Beard 1986; Parlak et al. 2000; Greene et al. 2006; Coltorti et al. 2007; Jagoutz et al. 2011). Importantly for its development as a single-mineral oxybarometer, Fe^{3+} and Fe^{2+} are both compatible in amphibole's octahedral sites (i.e., D $\geq$ 1 for at least one octahedral site; e.g., Dalpé and Baker 2000). A previous experimental study (King et al. 2000) found that Fe^{3+} partitioning into amphibole has a strong dependence on melt oxygen fugacity and kept pressure, temperature, and composition constant. In this contribution, we calibrate the Fe^{3+}/Fe^{2+} of

* Present address: School of Earth and Space Exploration, Arizona State University, 781 Terrace Mall, Tempe, AZ 85287, U.S.A. E-mail: aegoltz@asu.edu. Orcid 0000-0002-7282-1604
† Orcid 0000-0001-9486-8908

0003-004X/22/0011–2084$05.00/DOI: https://doi.org/10.2138/am-2022-8031

Table 1. Compositions and descriptions of starting mixes in wt% oxide

Mix no.	Description	Na_2O	MgO	Al_2O_3	SiO_2	MnO	FeO	K_2O	P_2O_5	TiO_2	CaO
53	3600 Tephra parent	2.66	13.19	12.86	52.80	0.20	8.20	1.49	0.00	0.77	7.83
54	7600 Tephra parent	2.76	16.32	12.72	52.10	0.17	8.02	0.54	0.21	0.62	6.56
59	7600 Tephra	3.27	9.49	16.04	54.00	0.19	7.50	0.66	0.21	0.75	7.89
60	3600 Tephra	2.74	10.83	13.73	52.56	0.20	8.63	1.64	0.36	0.81	8.51
61	Soufriere Hills andesite	3.66	2.71	17.49	60.64	0.20	7.11	0.69	0.00	0.61	6.92
BB	Black Butte dacite	4.70	2.14	17.50	65.62	0.04	3.20	1.14	0.00	0.43	5.23

igneous amphibole as an indicator of magmatic oxygen fugacity at arc settings using experimentally determined amphibole-melt partition coefficients at a wide range of pressures, temperatures, and compositions applicable to arc settings. We then apply our oxybarometer to amphibole in cumulate, tephra, and mafic enclave samples collected from Shiveluch Volcano, Kamchatka, and, using the samples previously reported whole rock chemistries and petrography, interpret the primitive oxygen fugacity of this volcano to be ~NNO+2. Insight into the volcano's plumbing system is also gained by calculating and comparing the variable residence time of amphiboles in several mafic enclaves.

Methods

Starting material

Experiments were conducted on five different synthetic bulk compositions: four basaltic and one andesitic (Table 1). Two of the basaltic compositions are equivalent to the major element composition of tephra erupted at Shiveluch volcano 3600 and 7600 BP (e.g., Volynets et al. 1997; Ponomareva et al. 2007) and differed predominately in their potassium contents. The other two basaltic compositions are calculated parental magmas to the tephra compositions. The parental composition of the 3600 BP tephra was calculated by Gavrilenko et al. (2016) by adding olivine back to the original tephra composition with a variable K_D until it reached equilibrium with Fo_{90} olivine. The parental composition of the 7600 BP tephra was calculated by iterative addition of olivine in 1 wt% steps assuming a $K_D = 0.32$

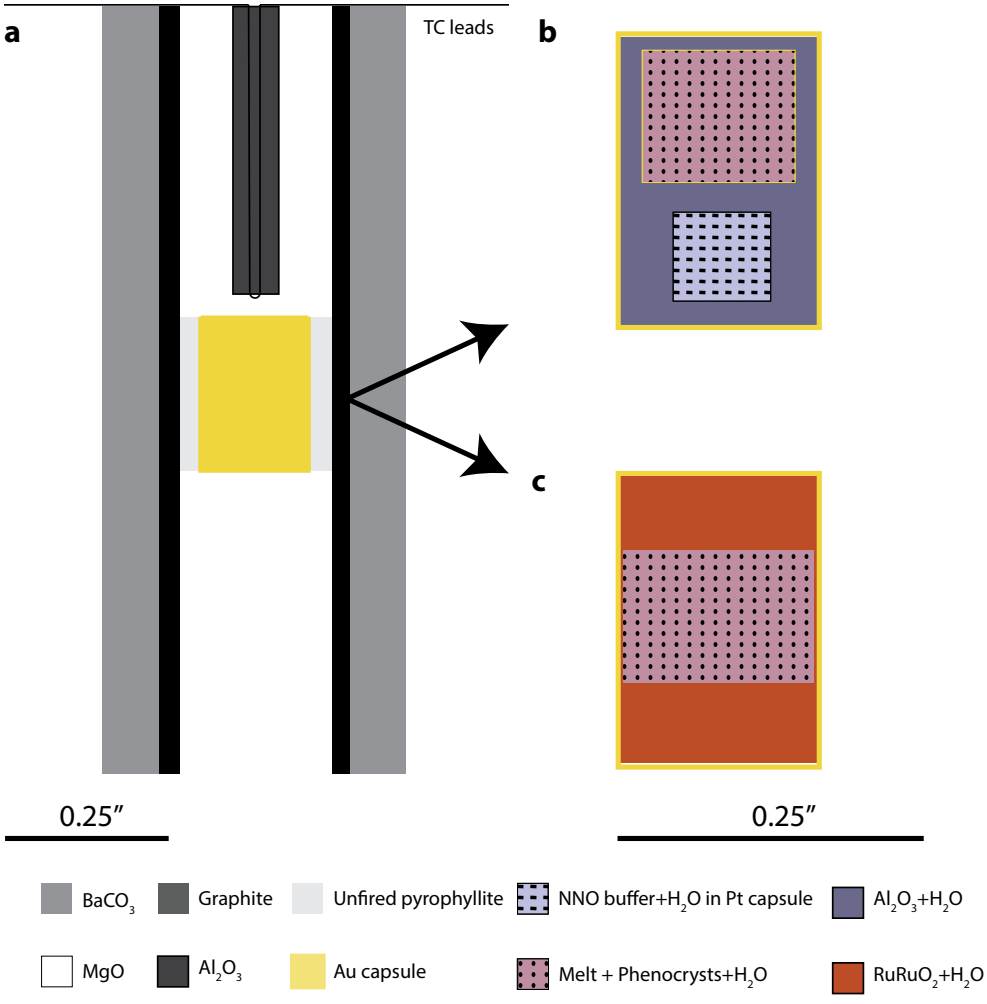

Figure 1. (**a**) Assembly for ½″ piston-cylinder experiments. ¾″ piston-cylinder assembly is not shown, but differs in the larger inner diameter of the graphite furnace (and, correspondingly, the outer diameter of MgO parts), taller height, substitution of $BaCO_3$ for NaCl as a pressure medium, and addition of Pyrex glass sleeve separating pressure medium and graphite furnace. (**b** and **c**) Capsule designs for experiments buffered at NNO or Ru-RuO_2, respectively. (Color online.)

and all iron as Fe^{2+}, until it reached equilibrium with olivine of Fo_{90}. The andesitic composition is the Soufriere Hills dome sample MVO34 (Barclay et al. 1998).

Synthetic mixes were made by combining simple oxides, carbonates (Na_2CO_3, K_2CO_3), hydroxides [$Mg(OH)_2$], and silicates ($CaSiO_3$). Iron was added to the mixes using both Fe_2O_3 and Fe^0 sponge in equal molar proportions. The Fe^0 sponge was added to the mixes after an initial homogenization step using a silicon-nitride ball mill filled with isopropanol. The mix, including the Fe^0 sponge, was gently ground by hand in an agate mortar until enough isopropanol had evaporated so that the metal particles would not separate by density. Material used in high-pressure experiments was pre-conditioned at the nickel-nickel oxide buffer (NNO) by suspending the mix (bound with polyvinyl alcohol) on a thin (0.2 mm diameter) Pt wire in a CO_2-H_2 Deltech gas mixing furnace at 1000 °C for ~24 h.

Experimental procedures

All experiments were run using piston-cylinder apparatuses at Washington University in St. Louis. Two experimental assemblies were used depending on the pressure of the experiments. For 500 MPa experiments, an assembly with a 19.1 mm outer diameter with NaCl pressure medium, Pyrex-glass inner sleeve, and graphite furnace was used. Experiments at 1 GPa an assembly with a 12.5 mm outer diameter, with a thin piece of Pb-foil around the outside for lubrication, $BaCO_3$ as the pressure medium and a graphite furnace (Fig. 1a). Experiments were first pressurized to the target experimental pressure and then heated at 50 °C/min to 865 °C for a dwell of 6 min and then heated at the same rate to the target temperature. Temperature was monitored using a Type C thermocouple and controlled within 5° of the target temperature using a Eurotherm PID controller. Experiments were quenched by turning off the power while maintaining experimental pressure (isobaric quench). Run times for all experiments were ~48 h (Table 2).

All experiments run at NNO used a triple capsule design (Fig. 1b). Twenty milligrams of a 5:1 mixture of Ni:NiO was packed in a Pt capsule with 2–3 µL of deionized water; the capsule was then crimped and welded shut using a TIG welder cooled under Argon gas. A gold sample capsule welded and flattened on one end was packed with 30 mg of sample and 6 µL of deionized water for water-saturated runs or 2 µL for water undersaturated runs, and it was then crimped, welded shut, and flattened. Both the sample and the buffer capsules were packed in a larger diameter outer Au capsule flattened and welded on one end. In addition to the Au sample and Pt buffer capsules, the outer Au capsule contained 20 µL of deionized water for water-saturated runs or 2 µL for water undersaturated experiments and powdered Al_2O_3. The powdered alumina made the sample extraction process after the experiment easier because the three capsules did not pressure weld together. The outer capsule was then crimped, welded, and flattened.

Experiments run at the ruthenium-ruthenium oxide buffer (Ru-RuO_2) used a single capsule design based on that described in Zhang et al. (2018) (Fig. 1c). The Ru-RuO_2 buffer is a relatively oxidizing buffer at high pressures (close to magnetite-hematite; O'Neill and Nell 1997). Neither ruthenium nor ruthenium oxide reacts with or is soluble in silicate melts, meaning that the buffer can be in direct contact with the sample, thus obviating the need for water saturation to buffer experiments at this oxygen fugacity. In the single capsule design, water and sample were sandwiched between two layers of buffer in a gold capsule, which was then crimped, welded, and flattened.

Water loss from the capsule during welding was monitored by weighing before and after welding; in all cases, water loss was within the analytical uncertainty of the balance (0.1 mg). The capsule's seal was evaluated by weighing before and after heating in a 300 °F oven for 1–2 min. If weight loss was ≥0.5 mg, the capsule was reinspected, rewelded, reweighed, and reheated to check for an improvement in the seal. The total loss of water from the capsule was never >2 mg (i.e., 2 µL). The presence of water in the capsule after the experiment was assessed by drilling a small hole into the capsule, releasing free water. The presence of the buffering assemblage (Ni-NiO or Ru-RuO_2) was also confirmed at the end of the experimental run by inspection of the platinum capsule (Ni-NiO) or by inspection in thin section using backscattered electron microscopy (BSE).

Analytical methods

Electron probe microanalysis (EPMA). Microprobe analysis of natural and synthetic amphibole was performed on a JEOL JXA-8200 electron microprobe equipped with five wavelength-dispersive spectrometers. Analyses were acquired using the Probe for EPMA software (Donovan et al. 2012); background correction was performed using a mean atomic number (MAN) correction (Donovan and Tingle 1996); and corrections for atomic number, X-ray absorption, and secondary fluorescence (ZAF) were performed using the CITZAF software (Armstrong et al. 2013). Analytical conditions for sample analyses were: 15 kV accelerating potential, 1–3 µm beam diameter for minerals and 10–30 µm for glasses, and 25 nA beam current.

The instrument was standardized for the analysis of Si, Ti, Mg, Al, Mn, Fe, Cr, Ni, Ca, Na, and K before the run using natural primary standards: Amelia albite, Gates wollastonite, Elba hematite, Madagascar orthoclase, Durango apatite, and pyrite and synthetic forsterite, Mn-olivine, Ni-olivine, chromite, and rutile. Other secondary standards were used for the MAN correction (e.g., Donovan et al. 2012). Na and K were analyzed in the first 20 s (for K) to 45 s (for Na) using TAP and PETJ crystals, respectively, to mitigate the effects of alkali migration during analysis. For analyses of glass with beam sizes <10 µm, a 10 nA beam current was used and a time-dependent intensity analysis (TDI) procedure was applied to determine the concentrations of Na and Si in the glass before beam damage. The TDI correction mitigates the effect of beam damage on Na and Si migration by using a linear regression fit to the log intensity of the element vs. time at 9 s intervals to determine the log intensity (and, by extension, concentration) initially. The accuracy of the standardization was verified by periodic analyses of the secondary standard Kakanui hornblende throughout the analytical session.

X-ray absorption fine structure. Samples were analyzed over the course of two sessions at beamline 13-IDE at the Advanced Photon Source at Argonne National Lab and one session at Beamline 4-BM at the National Synchrotron Light Source II at Brookhaven National Lab. The Fe *K*-edge spectra were scanned from 7012–7356 eV in fluorescence mode. From 7012–7100 eV, the resolution was 2.5 eV; from 7100–7142 (which includes the pre-edge and main absorption peak energies), a higher resolution of 0.1 eV was used; from 7142–7160, the resolution

TABLE 2. Experimental conditions and phase relations

ID	Starting mix	*T* (°C)	*P* (GPa)	f_{O_2}	CH_2O (wt%)	*t* (h)	Phase (%)
OD143	60-hiK tephra	1060	1	NNO	12.33	48	gl(51)+cpx(24)+amph(11)+opx(11)
OD144	59-loK tephra	1060	1	NNO	8.92	48	gl(67)+amph(13)+opx(16)+cpx(4)
OD102	53-hiK parent	1050	1	NNO	20.17	48	gl(58)+cpx(18)+am(7)+ol(17)
F136	53-hiK parent	1010	1	NNO	19.74	47	gl(45)+am(31)+ cpx(13)+ol(11)
F137	54-loK parent	1010	1	NNO	19.78	48	gl(47)+ol(21)+am(32)
F163	60-hiK tephra	1000	1	NNO	19.56	48	gl(46)+am(38)+cpx(10)+ol(2)+opx(2)
F178	**60-hiK tephra**	**1000**	**1**	**$RuRuO_2$**	**19.56**	**48**	**am(54)+gl(41)+tmnt(4)+cpx(tr)**
OD109	59-loK tephra	1000	1	NNO	19.32	52	gl(58)+am(40)+opx(2)
OD138	60-hiK tephra	1000	1	$RuRuO_2$	17.7	45	am(58)+gl(36)+tmnt(5)+phos(tr)
F174	**60-hiK tephra**	**950**	**0.5**	**NNO**	**10.16**	**48**	**am(63)+gl(34)+opx(2)+phos(1)**
F177	61-Soufriere andesite	950	0.5	NNO	9.78	48	gl(86)+plag(8)+amph(6)+opx(tr)
F179	**60-hiK tephra**	**950**	**1**	**$RuRuO_2$**	**18.73**	**48**	**am(60)+gl(37)+tmnt(4) (results calculatedwithout sodium)**
OD129	61-Soufriere andesite	950	1	NNO	18.47	48	gl(99)+am(1)+tmnt(tr)
F176	61-Soufriere andesite	900	0.5	NNO	9.44	49	gl(92)+am(8)+plag(tr)+unreacted corundum
MC69	Black Butte dacite	900	0.3	NNO+1	6.75	48	gl+plag+am+ox
OD131	61-Soufriere andesite	900	1	NNO	17.37	49	gl(85)+am(15)+tmnt(tr)
OD139	61-Soufriere andesite	900	1	$RuRuO_2$	17.37	48	gl(73)+plag(15)+tmnt(6)+am(5)
MC48	Black Butte dacite	875	0.2	NNO+1	5.46	48	gl+plag+am+opx+cpx+ox
MC49	Black Butte dacite	850	0.2	NNO+1	5.41	456	gl+plag+am+opx+cpx+ox
MC68	Black Butte dacite	850	0.3	NNO+1	6.53	96	gl+plag+am+opx+cpx+ox
MC51	Black Butte dacite	825	0.2	NNO+1	5.34	312	gl+plag+am+opx+cpx+ox

Note: Bolded experiments report TDI-corrected glass compositions (see Analytical Methods).

was 2 eV; and from 7160–7356, the resolution was 3 eV. The beam was focused to a 3–5 µm diameter using Kirkpatrick-Baez mirrors.

Natural and synthetic amphiboles were analyzed *in situ* in thin section. The orientation of amphibole affects the spectral intensity and shape of X-ray absorption fine structure (XAFS) spectra because of its anisotropy (e.g., Delaney et al. 1996; Dyar et al. 2016). To account for the unknown crystallographic orientation of analyzed grains in this study, the Fe^{3+}/Fe_{Total} of amphibole was determined using partial least squares, a multivariate regression technique, using the Data Exploration, Visualization, and Analysis for Spectroscopy (DEVAS) website at nemo.mtholyoke.edu (Carey et al. 2017). A predictive model using 186 spectra of oriented and unoriented amphibole Fe^{3+}/Fe_{Total} standards from a previous study (Dyar et al. 2016) was generated using the least absolute shrinkage and selection operator (Lasso). Spectra were pre-processed by normalizing intensities to 1 at 7350 eV and by applying a Kajfosz-Kiwiatek baseline correction (bottom width = 100, top width = 26; Kajfosz and Kwiatek 1987). The model was cross-validated for 14 folds. The model with the lowest mean squared error ($\alpha = 0.0001319$ for this model) was used to predict unknown amphibole Fe^{3+}/Fe_{Total}. The root mean square error of cross validation (RMSE-CV) of this model is taken as the accuracy of the predictions of Fe^{3+}/Fe_{Total} of amphibole unknowns; in our model, the RMSE-CV was ±10.8. The root mean square error of calibration (RMSE-C, describing the model's ability to reproduce the Fe^{3+}/Fe_{Total} of standards) of this model was ±4.7 ($R^2 = 0.963$). See Dyar and Ytsma (2021) for more information on these accuracy measures.

Results

Experimental observations and evidence of equilibrium

Phase relations and average phase compositions in our experiments are reported in Table 2 and Online Materials[1] Table S1, respectively. Phase proportions were calculated by mass balance using starting compositions, average phase compositions, and the mass balance program LIME (Krawczynski and Olive 2011; Prissel et al. in prep). The mass balance calculations show that experimental run products are deficient in Na_2O compared to the bulk starting material. In some cases, this deficit is as high as 77% of the total Na_2O. Because the experiments were run at fluid-saturated conditions, and a fluid phase would preferentially scavenge sodium, we believe that the unaccounted-for sodium was dissolved in this phase. Another possibility to explain the low-Na_2O concentrations in the synthetic minerals and glass is sodium migration during EPMA analysis. This effect would be most pronounced in high-sodium glass and plagioclase, and our hydrous glasses are sensitive to electron beam damage. While this possibility cannot be discounted as contributing to apparent sodium loss, it is not likely the sole factor controlling the sodium deficit in experimental phases because our analytical conditions (large beam diameter and TDI corrections) were chosen to minimize the effects of sodium migration.

Water contents of glasses in water-saturated experiments were calculated using the equations of Papale et al. (2006), assuming XH_2O in the fluid phase was equal to 1. For 1 GPa experiments, the water content was calculated to be 17–20 wt%, and for 0.5 GPa experiments, the water content was calculated to be about 10 wt% (Table 2). The water content of water-undersaturated experiments was calculated using the percent glass and the amount of water added to the capsule at the start of the experiment. As a result of the high water contents [which far exceed the "quenchability limit" of glass found by Gavrilenko et al. (2019)], experimental glass is vesicular and frothy (Fig. 2). The quenchability limit of glass is 9 ± 1 wt% in basaltic glasses, which is consistent with low EPMA analytical totals in our experimental glasses (Online Materials[1] Table S1), and the frothy and vesicular nature of the glass may also contribute to low EPMA totals. Especially for water-saturated experiments with experimental water contents significantly greater than 9 wt%, the deficit from 100 wt% of these totals cannot be interpreted as the water content of the melt.

Amphibole and glass are the two most abundant phases in most experiments. At higher temperatures, olivine and pyroxene are also stable. Due to the high-water content of the experiments, plagioclase was not a major crystallizing phase in experiments at 1 GPa but was present in three experiments run on andesite starting compositions. Two of the three—F177 and F176—were run at 0.5 GPa (Table 2); the lower water content of these experiments may have allowed plagioclase to crystallize closer to the liquidus. The third experiment was run at a relatively low temperature and was buffered at relatively high f_{O_2} (an experiment run at intermediate f_{O_2} at the same pressure and temperature conditions did not have equilibrium plagioclase). Plagioclase has been shown to crystallize at higher temperatures at more oxidizing conditions (e.g., Hamilton et al. 1964), which would explain its presence in the higher f_{O_2} experiment.

Attainment of equilibrium in these experiments is suggested by crystal morphology, homogeneous crystal chemistry, and Fe/Mg equilibrium partitioning ratios for olivine and pyroxene. Silicate crystal size varies from ~5 to >100 µm (although smaller crystals were more common; Fig. 2). Crystals are euhedral and unzoned. Coupled with the relatively low standard deviation between glass analyses within a single experiment (Online Materials[1] Table S1), the geochemical data suggest equilibrium growth. The Fe/Mg distribution coefficients for olivine and clinopyroxene (all calculated assuming all iron as ferrous) from experiments buffered at NNO are 0.26–0.35 for olivine and 0.21–0.22 for clinopyroxene, which is within uncertainty of what is to be expected from other studies (Sisson and Grove 1993; Sugawara 2001; Kushiro and Mysen 2002; Putirka 2008; Bédard 2010), and would also suggest growth at equilibrium conditions.

Summary of synthetic amphibole and glass major element compositions

In addition to analyzing amphibole and glass in our piston-cylinder experiments conducted on basaltic and andesitic compositions, we also analyzed amphiboles from experiments previously reported in McCanta et al. (2007), conducted on a dacitic starting composition at lower pressures (<500 MPa) using a cold-seal Waspaloy pressure vessel or an internally heated pressure vessel and an oxygen fugacity of NNO+1. All amphiboles in our experiments are solid solutions between tschermakite and pargasite end-members on the basis of their major element compositions and the classification scheme of Leake et al. (1997, 2003). The amphiboles are calcic, with ≥1.5 pfu calcium in the B site, and are dominantly magnesian with $Mg/(Mg+Fe^{2+}) > 0.5$. Si pfu varies from 6.2 to 6.6, and the A-site occupancy by sodium and potassium ranges from 0 to 0.78. There is no discernable trend in Al, Ca, Ti, or Na with decreasing Mg pfu in amphibole, but experiments run at the Ru-RuO_2 buffer tend to be relatively lower in Ti and Na (Fig. 3). Glass in our experiments is basaltic andesite to dacite in composition when normalized to 100 wt% on an anhydrous basis.

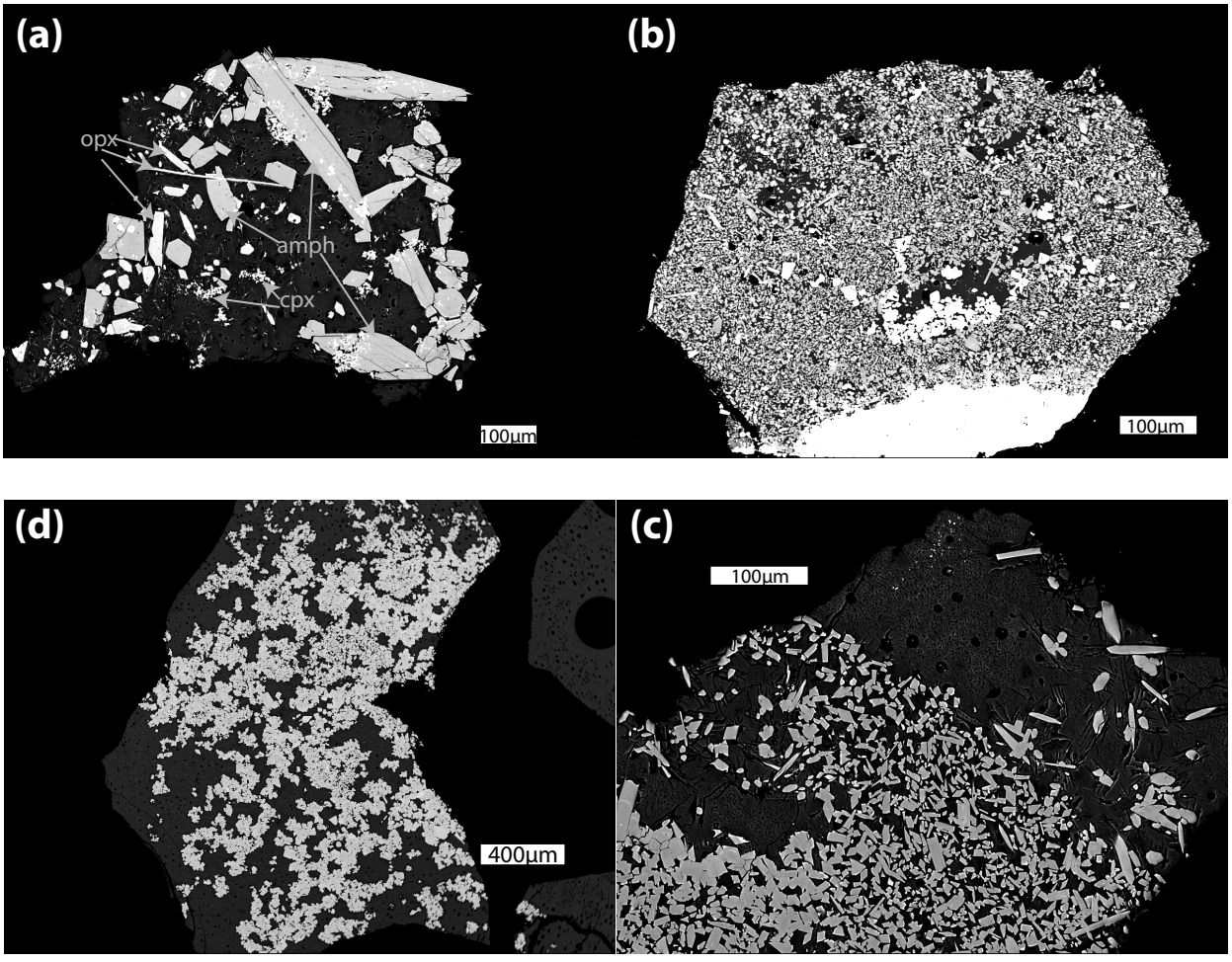

Figure 2. BSE images of experimental products (**a**) F163, (**b**) F179, (**c**) OD109, and (**d**) OD129. Crystalline phases are labeled in **a**. Relatively high-Z phases in **b** (i.e., bright phases) are titanomagnetite and, at the edge of the grain, Ru and RuO_2 (the buffering assemblage). Crystalline phase in **c** and **d** is amphibole.

Fe^{3+} and Fe^{2+} partitioning in amphibole

Fe^{3+} and Fe^{2+} amphibole-melt partition coefficients were determined using our XAFS analyses of amphibole and calculated Fe^{3+}/Fe^{2+} ratios of glasses. For amphibole, the Fe^{3+}/Fe_{Total} determined by XAFS analysis (as described in the methods section) and total molar iron from EPMA were used to determine Fe^{3+} and Fe^{2+}. We did not measure the Fe^{3+}/Fe^{2+} ratio of coexisting glass in these experiments and instead calculated them using Equation 7 of Kress and Carmichael (1991). Other studies (e.g., Sisson and Grove 1993; Moore et al. 1995; King et al. 2000; Gaillard et al. 2001; Wilke et al. 2002; Botcharnikov et al. 2005; Zhang et al. 2016) have shown good agreement between measured Fe^{3+}/Fe^{2+} of glass and calculated values for both hydrous and anhydrous glasses. Additionally, due to their very high water contents, glasses in our experiments are more prone to oxidation during measurement by XAFS, and, as an effect, reliable, direct measurements of them are more difficult (Cottrell et al. 2018; Blundy et al. 2020). It is notable that two glasses with >8 wt% H_2O analyzed by Blundy et al. (2020) using XAFS did not measure Fe^{3+}/Fe_{Total} equal to the predicted Fe^{3+}/Fe_{Total} value from the equation of Kress and Carmichael (1991). However, Blundy et al. (2020) did not find systematic changes in Fe^{3+}/Fe_{Total} with water content, and the two data points cannot be interpreted as conclusive evidence that the Kress and Carmichael (1991) equation is not applicable to glasses with very high-water content. For each experiment, the Fe^{3+} and Fe^{2+} of melt in equilibrium with amphibole were calculated using the composition of the equilibrium glass, experimental pressure, and temperature, and experimental oxygen fugacity from the equations of O'Neill and Pownceby (1993) for NNO and O'Neill and Nell (1997) for Ru-RuO_2.

Partition coefficients of Fe^{3+}, Fe^{2+}, Mg, and Fe^{2+}/Mg for each experiment are presented in Table 3 and a summary of average partition coefficients correlated with oxygen fugacity and starting composition is found in Table 4. The amphibole-melt Fe^{3+} partition coefficient ($D^{Fe^{3+}}$) does not vary with temperature, pressure, or melt composition (quantified as non-bridging oxygen (NBO) divided by tetrahedrally coordinated cations (T); Mysen 1988), but on average, experiments run at the Ru-RuO_2 buffer (i.e., high oxygen fugacity) have a higher $D^{Fe^{3+}}$ than experiments run at

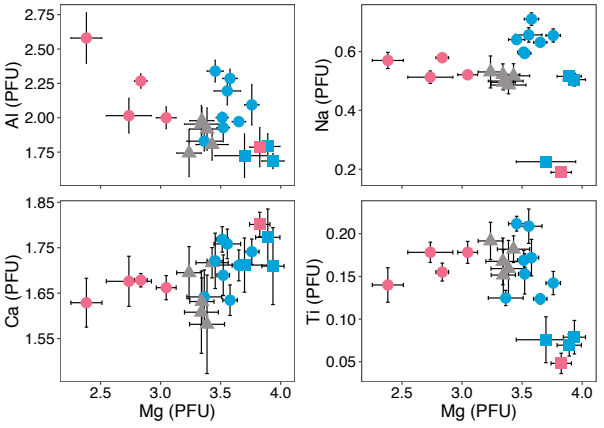

Figure 3. Amphibole major element variation diagrams. Color indicates starting composition (blue is basalt, pink is andesite, and gray is dacite) and shape indicates experimental f_{O_2} (circles are NNO, triangles are NNO+1, and squares are Ru-RuO_2). There is no discernable trend in major element chemistry with decreasing Mg, but experiments run at higher f_{O_2} are relatively lower in Ti, and some are lower in Na. (Color online.)

NNO or NNO+1. This is consistent with behavior described in King et al. (2000), who noted a difference between the partitioning of Fe^{3+}/Fe_{Total} at high-oxygen fugacities and oxygen fugacity near NNO (Figs. 4, 5, and 6). Not including experiments run at Ru-RuO_2, the average $D^{Fe^{3+}}$ for all starting compositions is 2.66 ± 0.57 (2 times standard error, 2SE); for high-f_{O_2} experiments at Ru-RuO_2 it is 3.88 ± 0.51.

The amphibole-melt Fe^{2+} and Mg partition coefficients ($D^{Fe^{2+}}$ and D^{Mg}) have a strong dependence on the structure, and by extension composition, of silicate melt but no correlation with pressure, water content, or oxygen fugacity (Figs. 4–6). Both partition coefficients increase with decreasing NBO/T. On average, for basalt at intermediate f_{O_2} (i.e., NNO and NNO+1), $D^{Fe^{2+}}$ is 1.18 ± 0.20; for andesites it is 2.34 ± 0.55; and for dacites it is 5.53 ± 1.24 (the quoted error is 2SE; Table 4). $D^{Fe^{2+}}$ has a weak dependence on temperature for experiments run on andesitic and dacitic starting compositions. The amphibole-melt Fe^{2+}/Mg distribution coefficient ($K^{Fe^{2+}/Mg}$, defined as $D^{Fe^{2+}}/D^{Mg}$) is independent of melt structure and has an average value across all experiments at intermediate f_{O_2} of 0.27 ± 0.02 (2SE).

The amphibole-melt distribution coefficient of the ferric ferrous ratio was also calculated from our data. We define this term, $K^{Fe^{3+}/Fe^{2+}}$, as:

$$K^{Fe^{3+}/Fe^{2+}} = \frac{\left(\frac{Fe^{3+}}{Fe^{2+}}\right)_{amph}}{\left(\frac{Fe^{3+}}{Fe^{2+}}\right)_{melt}}$$

We apply this ratio to determine the oxygen fugacity of natural samples from the ferric-ferrous ratio of amphibole because it is independent of the melt's total iron content. We exclude experiments run at the Ru-RuO_2 buffer from this calibration because the oxygen fugacity of those experiments is significantly higher than would be expected for natural arc magmas. On average, $K^{Fe^{3+}/Fe^{2+}}$ of basalts, andesites, and dacites at intermediate f_{O_2} (i.e., NNO-NNO+1) are 2.02 ± 0.31, 0.96 ± 0.14, and 0.62 ± 0.15, respectively (Fig. 6; Table 4).

XAFS measurements of amphiboles in natural samples

Natural samples in which amphibole was analyzed were all erupted from Shiveluch Volcano in the Kamchatkan arc. For full descriptions of samples besides the 3600 BP tephra, the reader is directed to Goltz et al. (2020); descriptions of the tephra may be found in Volynets et al. (1997) and Ponomareva et al. (2007). To summarize, all but samples 04L, 16B, and the 3600 BP tephra are amphibole and olivine-phyric quenched liquid cognate xenoliths (mafic enclaves) with basaltic-to-basaltic andesite bulk compositions that were erupted in pyroclastic flows mostly composed of andesite. Samples 04L and 16B are clinopyroxene and amphibole-rich cumulates. The 3600 BP

Table 3. Average amphibole Fe^{3+}/Fe^{2+}, glass Fe^{3+}/Fe^{2+}, and partition coefficients for each experiment with 1 sigma uncertainty

ID	f_{O_2}	Amph Fe^{3+}/Fe^{2+}	Glass Fe^{3+}/Fe^{2+}	$D^{Fe^{3+}}$	Sigma $D^{Fe^{3+}}$	$D^{Fe^{2+}}$	Sigma $D^{Fe^{2+}}$	D_{Mg}	$K^{Fe^{2+}/Mg}$	Sigma $K^{Fe^{2+}/Mg}$	$K^{Fe^{3+}/Fe^{2+}}$	Sigma $K^{Fe^{3+}/Fe^{2+}}$
OD143	NNO	0.47	0.19	2.29	0.77	0.95	0.15	3.86	0.25	0.04	2.41	0.90
OD144	NNO	0.47	0.19	2.64	0.89	1.06	0.17	4.43	0.24	0.04	2.49	0.93
OD102	NNO	0.44	0.19	2.33	0.83	1.01	0.16	3.95	0.26	0.04	2.30	0.89
F136	NNO	0.42	0.20	2.31	0.84	1.09	0.17	5.01	0.22	0.04	2.12	0.84
F137	NNO	0.36	0.19	2.05	0.84	1.06	0.16	3.53	0.30	0.05	1.93	0.84
F163	NNO	0.22	0.20	1.51	0.90	1.36	0.18	4.94	0.28	0.05	1.11	0.68
F178	$RuRuO_2$	14.00	4.45	3.46	0.40	1.10	1.78	8.77	0.13	0.22	3.15	5.11
OD109	NNO	0.42	0.20	2.22	0.82	1.07	0.16	4.43	0.24	0.04	2.08	0.83
OD138	$RuRuO_2$	10.79	4.45	4.25	0.50	1.75	2.23	13.06	0.13	0.30	2.42	3.10
F174	NNO	0.43	0.25	3.10	1.11	1.81	0.28	8.99	0.20	0.06	1.71	0.67
F177	NNO	0.27	0.24	2.04	1.02	1.79	0.25	6.35	0.28	0.07	1.14	0.59
F179	$RuRuO_2$	5.72	5.36	3.44	0.44	3.22	2.34	5.72	0.56	1.32	1.07	0.79
OD129	NNO	0.17	0.21	1.71	1.28	2.11	0.27	6.45	0.33	0.09	0.81	0.62
F176	NNO	0.26	0.26	2.35	1.24	2.36	0.32	7.67	0.31	0.10	1.00	0.54
MC69	NNO+1	0.27	0.46	2.58	1.30	4.38	0.60	18.29	0.24	0.14	0.59	0.31
OD131	NNO	0.20	0.22	2.80	1.81	3.08	0.40	7.84	0.39	0.16	0.91	0.60
OD139	$RuRuO_2$	10.00	6.29	4.39	0.52	2.76	3.28	7.67	0.36	1.18	1.59	1.90
MC48	NNO+1	0.21	0.50	1.91	1.19	4.52	0.59	17.05	0.26	0.16	0.42	0.27
MC49	NNO+1	0.31	0.52	3.68	1.67	6.10	0.87	28.52	0.21	0.19	0.60	0.29
MC68	NNO+1	0.31	0.50	3.09	1.40	4.96	0.70	16.71	0.30	0.21	0.62	0.30
MC51	NNO+1	0.48	0.54	6.74	2.26	7.70	1.23	27.61	0.28	0.34	0.88	0.32

Notes: Uncertainty was propagated analytically through the calculation of the partition coefficients for each experiment using the uncertainty of the DEVAS calibration and the standard deviation of average compositions for glass and amphibole from EPMA.

TABLE 4. Mean and 2 standard error (SE) of $D^{Fe^{3+}}$, $D^{Fe^{2+}}$, D_{Mg}, $K^{Fe^{2+}/Mg}$, and $K^{Fe^{3+}/Fe^{2+}}$ for all intermediate f_{O_2} experiments (i.e., experiments conducted at NNO and NNO+1), high-f_{O_2} experiments (i.e., experiments conducted at Ru-RuO_2), and intermediate f_{O_2} experiments with basalt, andesite, or dacite starting compositions separately

Starting composition	Oxygen fugacity	No. experiments	$D^{Fe^{3+}}$	2SE	$D^{Fe^{2+}}$	2SE	D_{Mg}	2SE	$K^{Fe^{2+}/Mg}$	2SE	$K^{Fe^{3+}/Fe^{2+}}$	2SE
All	Intermediate	17	2.66	0.57	2.73	1.00	10.33	3.99	0.27	0.02	1.36	0.35
All	Ru-RuO_2	4	3.88	0.51	2.21	0.96	8.80	3.10	0.30	0.21	2.06	0.92
Basalt	Intermediate	8	2.30	0.32	1.18	0.20	4.89	1.22	0.25	0.03	2.02	0.31
Andesite	Intermediate	4	2.22	0.46	2.34	0.55	7.08	0.79	0.33	0.05	0.96	0.14
Dacite	Intermediate	5	3.60	1.67	5.53	1.24	21.64	5.28	0.26	0.03	0.62	0.15

Note: 2SE is calculated by dividing the standard deviation of the average for each group by the square root of the number of experiments in that group, and then multiplying that quantity by two.

tephra is one of two basaltic tephra erupted from Shiveluch and contains amphibole and phlogopite phenocrysts. The composition of this tephra has been hypothesized to be representative of a magmatic composition parental to the less magnesian mafic enclaves (e.g., Volynets et al. 1997; Goltz et al. 2020). Both the tephra and mafic enclaves show evidence for coexistence of high-Mg# amphibole (i.e., Mg# > 74) and high-forsterite olivine (i.e., $Fo_{90–92}$), which implies crystallization from a super-hydrous primary magma, with an estimated primary magmatic water content ranging up to 10 wt% H_2O. Magmas at Shiveluch are primarily products of flux melting of the mantle overlying the subducting Pacific plate. Other possible contributions to primary magmas at Shiveluch include melting of a hydrous pyroxenite upper mantle layer (KUMA; Nikulin et al. 2010, 2012), slab melting caused by an underlying slab tear (e.g., Peyton et al. 2001; Yogodzinski et al. 2001; Park et al. 2002; Levin et al. 2002; Jiang et al. 2009), and melting of the subducting Emperor Seamounts (e.g., Nishizawa et al. 2017).

Amphibole in the enclaves spans a relatively wide range of Fe^{3+}/Fe_{Total}, from 16.7 to 84.1% (excluding statistical outliers; Table 5). The Fe^{3+}/Fe^{2+} of amphibole analyzed in natural samples is summarized by sample in Figure 7. The summarized data set excludes analyses from within 500 µm of amphiboles that were highly oxidized (i.e., predicted $Fe^{3+}/Fe_{Total} > 90\%$). Highly oxidized amphiboles were observed in three contexts within our samples: the oxidized andesite surrounding the mafic enclaves, the contact between the enclave or cumulate and the andesite, and a single isolated grain in the tephra. The Fe^{3+}/Fe^{2+} ratio of these amphiboles is not representative of magmatic oxidation states and most likely reflects post-crystallization oxidation during eruption or magma mixing. Excluded analyses and images may be found in the Online Materials[1] data, but further discussion of these analyses is beyond the scope of this contribution.

Because amphiboles in these natural samples are commonly zoned in major elements (i.e., Mg#, Al_2O_3), we investigated the possibility of zoning in Fe^{3+}/Fe_{Total} by analyzing multiple points in single grains. The criterion for statistically significant zoning is an intracrystalline compositional variation greater than twice the accuracy of the model used to determine amphibole Fe^{3+}/Fe_{Total} ($\sigma \approx 11$, see Methods section). Only eight crystals of >69 analyzed grains met this criterion. Zoning in these grains is irregular and is not continuous from core to rim. Neither amphibole Mg# nor Al_2O_3 correlates with Fe^{3+}/Fe_{Total} in these grains. Because of the irregularity of the zoning profiles, the lack of correlation with other elements, and that often one analysis point in each of these crystals is responsible for their qualification as zoned, we take these zoned crystals to be outliers in our larger data set.

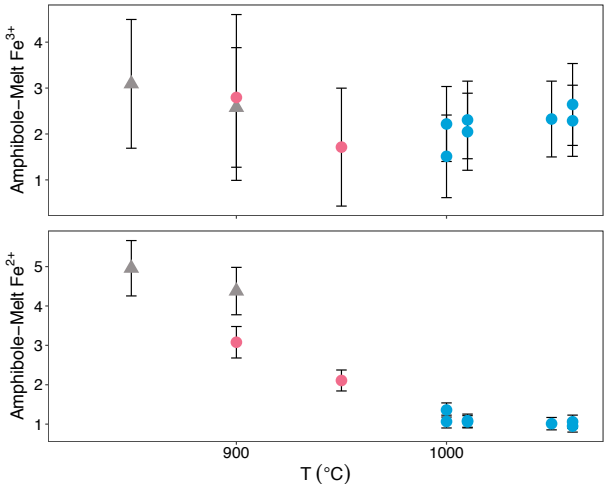

FIGURE 4. Plot showing experimental temperature vs. $D^{Fe^{3+}}$ and $D^{Fe^{2+}}$. For each starting composition, results from only 1 experimental pressure and oxygen fugacity are shown (1 GPa and NNO for basalts and andesites, and 300 MPa and NNO+1 for dacite). There is no apparent effect of temperature on the partitioning of Fe^{3+} or Fe^{2+}, but Fe^{2+} partitioning has a weak temperature dependence in experiments with andesitic and dacite starting compositions. Color and shape are as in Figure 3. (Color online.)

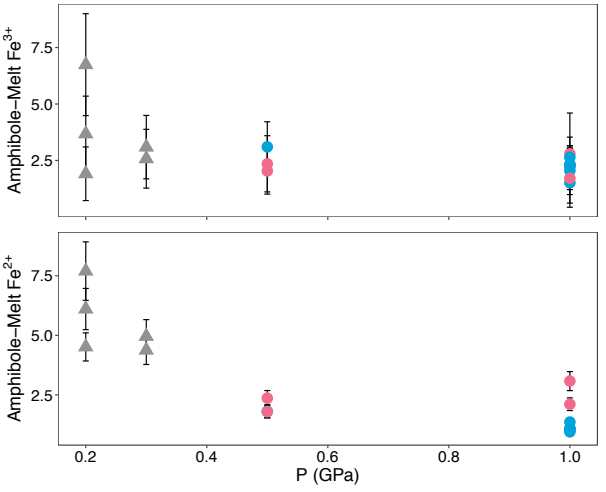

FIGURE 5. Experimental pressure vs. $D^{Fe^{3+}}$ and $D^{Fe^{2+}}$. There is no discernable effect of pressure on the partitioning of Fe^{3+} or Fe^{2+}. Color and shape are as in Figure 3. (Color online.)

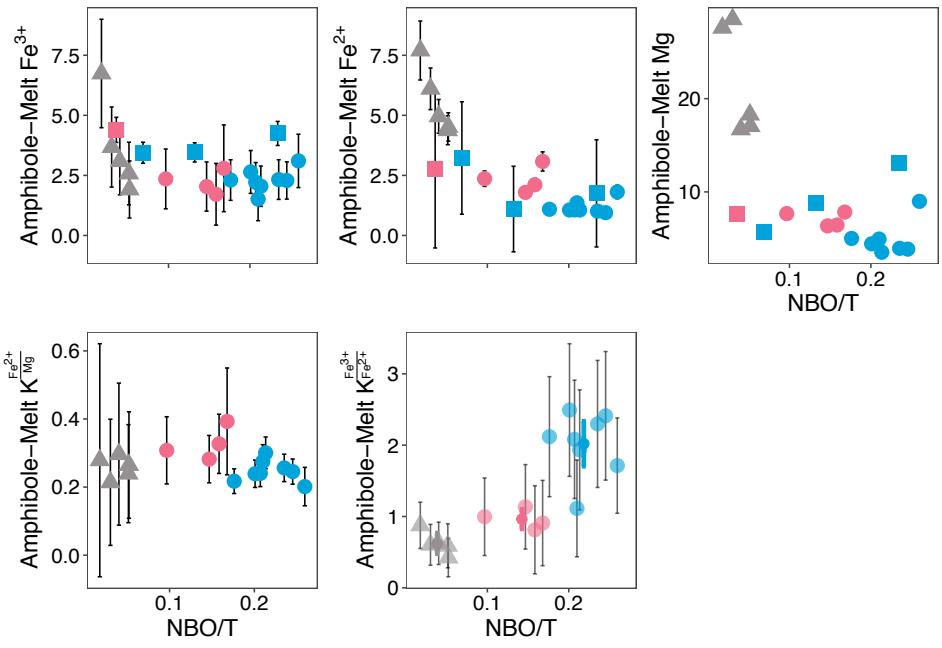

Figure 6. Melt NBO/T vs. $D^{Fe^{3+}}$, $D^{Fe^{2+}}$, DMg, $K^{Fe^{2+}/Mg}$, and $K^{Fe^{3+}/Fe^{2+}}$. NBO/T was calculated using the procedure in Mysen (1988) on an anhydrous basis. Melt polymerization has a significant effect on Fe^{2+} partitioning and appears to have an exponential relationship with the partition coefficient. Oxygen fugacity has a minor effect on the partitioning behavior of Fe^{3+}. Color and shape are as in Figure 3. The thick bars in the plot of $K^{Fe^{3+}/Fe^{2+}}$ represent the average partition coefficient for each starting composition, excluding experiments done at the Ru-RuO_2 buffer. Because the high-f_{O_2} experiments are only indirectly relevant to arc settings, we excluded them from plots showing $K^{Fe^{2+}/Mg}$ and $K^{Fe^{3+}/Fe^{2+}}$. (Color online.)

Discussion

Fe^{3+} partitioning between amphibole and melt

Results from our experiments show that Fe^{3+} is compatible in amphibole (i.e., $D^{Fe^{3+}} > 1$). This result is consistent with predictions from lattice strain models (e.g., Dalpé and Baker 2000; Adam et al. 2007), partitioning data from King et al. (2000), and the wide range of Fe^{3+} observed in naturally occurring amphiboles (Dyar et al. 1992, 1993). The partitioning of Fe^{3+} between amphibole and melt is not affected by pressure, temperature, or melt composition; however, experiments buffered at high f_{O_2} (Ru-RuO_2) have a higher $D^{Fe^{3+}}$ than experiments buffered at intermediate f_{O_2} (NNO or NNO+1), on average (3.9 vs. 2.7). A similar relationship between f_{O_2} and Fe^{3+} partitioning between amphibole and melt was reported by King et al. (2000). The difference in $D^{Fe^{3+}}$ between experiments at different f_{O_2} might be an effect of changing Fe^{3+} behavior in the melt with changing oxygen fugacity. In their study of andesitic glass at variable f_{O_2}, Zhang et al. (2016) showed that Fe^{3+} became more network-modifying as its concentration increased (i.e., at higher f_{O_2}). The change in the behavior of Fe^{3+} in the melt may lead to the observed difference in its partitioning behavior.

The lower Na and Ti content of amphibole synthesized at high f_{O_2} relative to amphibole at lower f_{O_2} suggests a different substitution mechanism to accommodate the high relative amount of Fe^{3+} in amphibole under these conditions. The low-Na content of some amphiboles synthesized at the Ru-RuO_2 buffer would suggest that, at high oxygen fugacities, the substitution $Na_1Fe^{2+}_1Fe^{3+}_{-1}\square^{A}_{-1}$

Table 5. Mean amphibole Fe^{3+}/Fe^{2+}, calculated f_{O_2}, percent dehydrogenation, and residence times in andesite for samples from Shiveluch

Sample	No. points	Average amphibole Fe^{3+}/Fe_{total}	SD amphibole Fe^{3+}/Fe_{total}	Average amphibole Fe^{3+}/Fe^{2+}	SD amphibole Fe^{3+}/Fe^{2+}	f_{O_2} (ΔNNO)	SD f_{O_2}	SE f_{O_2}	Percent Dehydrogenation	Median time (days)	Median time (months)	IQR (days)
16b	48	35.10	7.66	0.56	0.20	1.87	0.96	0.14				
3600 tephra	37	38.11	5.94	0.62	0.21	2.20	0.64	0.10				
09a	19	40.68	5.51	0.69	0.22	2.44	0.58	0.13	6.54	6	0.20	7.5
02b	21	42.34	5.96	0.75	0.24	2.62	0.65	0.14	8.41	11	0.25	11
06a	23	43.78	3.54	0.78	0.24	2.80	0.37	0.07	9.32	13	0.42	6.3
04l	29	46.30	4.51	0.87	0.27	2.99	0.46	0.08				
15f	31	47.54	7.26	0.93	0.29	3.06	0.72	0.13	14.3	31	1.0	19
5	24	51.14	6.54	1.07	0.33	3.47	0.67	0.14	20.4	64	2.1	35
04d	33	53.50	6.01	1.17	0.36	3.50	0.71	0.12	20.8	68	2.2	29
04b	40	53.79	6.22	1.19	0.37	3.58	0.67	0.10	21.0	69	2.3	26
04k	46	59.08	10.2	1.58	0.51	3.98	1.38	0.20	25.2	102	3.4	52

Notes: Uncertainty in f_{O_2} was calculated using a Monte Carlo approach, repeating the calculation 10 000 times with values normally distributed around the standard deviations of the amphibole Fe^{3+}/Fe^{2+} and the standard error of $K^{Fe^{3+}/Fe^{2+}}$ for intermediate basalts (see Table 4). The median and interquartile range of residence times were calculated using a similar approach, repeating the calculation 10 000 times with starting values normally distributed around the mean and 2SE of amphibole FeO and Fe^{3+}/Fe_{total} in the sample.

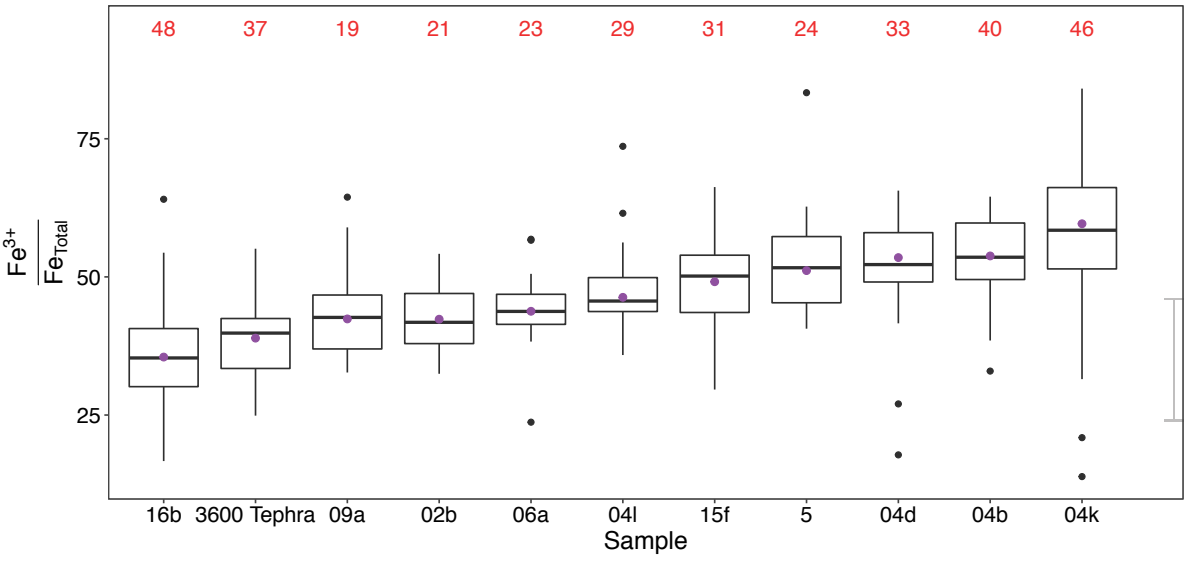

Figure 7. Box-and-whisker plot summarizing the median, interquartile range, minimum, and maximum values of Fe^{3+}/Fe_{Total} of amphiboles analyzed in mafic enclaves, cumulates, and tephra by sample. Statistical outliers are represented as black dots and were determined using the definition of McGill et al. (1978). Averages for each sample (excluding outlier points) are shown as purple points. The number of points represented by the box plot for each sample is shown in red. Gray error bar on far right represents accuracy of Fe^{3+}/Fe_{Total}. Analyses of oxidized crystals have been excluded from this summary. (Color online.)

may play a prominent role. This substitution mechanism was proposed first for dehydration of riebeckite (Ungaretti 1980) and then again for the dehydrogenation of igneous amphiboles (Phillips et al. 1988), but was found to be less important for Fe^{3+} substitution in natural amphiboles compared to substitutions involving other cations in the M1–3 sites and hydrogen in the O3 site (e.g., Dyar et al. 1993; Popp et al. 1995a; King et al. 1999). In our high-f_{O_2} experiments, substitution with A-site sodium may be necessary because of a structural limitation on the oxidation of the O3 site caused by preferential incorporation of Fe^{3+} over Ti in the M3 site (e.g., Hawthorne and Oberti 2007; Oberti et al. 2007). The relatively low-Ti content of amphiboles synthesized at high f_{O_2} may be related to the increased stability and abundance of titanomagnetite, which preferentially partitions Ti^{4+} from the melt at these more oxidizing conditions. Low-titanium amphiboles were also observed in equilibrium with titanomagnetite by King et al. (2000). Alternatively, the substitution mechanism $0.5H_2 + Ti^{4+} + O^{2-} \leftrightarrow Fe^{3+} + OH^-$ has been proposed as one of the dominant mechanisms for Fe^{3+} substitution in the past (e.g., Aoki 1963; Boettcher and O'Neil 1980; Dyar et al. 1992).

Fe^{2+} partitioning between amphibole and melt

Fe^{2+} is compatible in amphibole. It is relatively less compatible than Fe^{3+} for basalts and andesites and relatively more compatible in dacites, as evidenced by the compatibility of Fe^{2+} in amphibole increasing with decreasing NBO/T (Fig. 6). The compatibility of Fe^{2+} is also somewhat temperature dependent, as evidenced by a weak negative correlation with experimental temperature for andesite and dacite starting compositions. However, the temperature dependence of the Fe^{2+} partition coefficient could also be caused by changes in melt composition that invariably accompany changes in temperature, and we cannot distinguish these effects unequivocally from the data. The temperature dependence of $D^{Fe^{2+}}$ is less pronounced than its dependence on NBO/T.

The relationship between melt NBO/T and $D^{Fe^{2+}}$ can be modeled as an exponential (Fig. 6). NBO/T is also exponentially related to D^{Mg} in our experiments (Fig. 6). Similar exponential relationships between NBO/T and the amphibole-melt partition coefficients of large ion lithophile elements (LILE), rare earth elements (REE), and high field strength elements (HFSE) have been observed (e.g., Klein et al. 1997; Tiepolo et al. 2007). Notably, the Fe^{2+} and Mg mineral-melt partition coefficients of olivine and clinopyroxene have also been found to have exponential relationships with melt NBO/T (e.g., Kushiro and Mysen 2002; Toplis and Corgne 2002). The similar relationship between $D^{Fe^{2+}}$, D^{Mg}, and melt viscosity from this study of amphibole and from other studies of common silicate minerals suggests similar changes in the behavior of these elements with melt viscosity, as observed in our experiments.

In contrast to the exponential relationship of $D^{Fe^{2+}}$ and D^{Mg} with NBO/T, $K^{Fe^{2+}/Mg}$ (the ratio of $D^{Fe^{2+}}$ and D^{Mg}) is relatively constant (on average, 0.27; Fig. 6) and identical to the $K^{Fe/Mg}$ for clinopyroxene (Putirka 2008). The consistency of $K^{Fe^{2+}/Mg}$ in amphibole in our study is similar to the consistent $K^{Fe_{Total}/Mg}$ of olivine in the literature and stands in stark contrast to the relatively scattered $K^{Fe_{Total}/Mg}$ of amphibole in the literature (Fig. 8). The scatter in amphibole $K^{Fe_{Total}/Mg}$ has also been observed by Putirka (2016) who attributed it to a relatively slow rate of equilibration for amphibole; however, we view the scatter in amphibole $K^{Fe_{Total}/Mg}$ as highlighting the importance of considering Fe^{2+} when calculating distribution coefficients for minerals with Fe^{3+}. Other researchers have emphasized that the Fe-Mg distribution coefficient for olivine depends on the Fe^{3+}

content of olivine, and variability in the already well-constrained $K^{Fe_{Total}/Mg}$ for olivine is diminished when considering $K^{Fe^{2+}/Mg}$ instead (Blundy et al. 2020). The effect of considering Fe^{2+} in the calculation of the amphibole distribution coefficient is greater because Fe^{3+} is more compatible in amphibole than in olivine, and the difference between Fe_{Total} and Fe^{2+} must thus also be greater.

Application of $K^{Fe^{3+}/Fe^{2+}}$ as an oxybarometer

The utility of our experimentally determined $K^{Fe^{3+}/Fe^{2+}}$ as an oxybarometer is demonstrated by using it to calculate a range of magmatic f_{O_2} at Shiveluch volcano. The mean Fe^{3+}/Fe^{2+} of the melt in equilibrium with each of 11 samples was calculated by multiplying the average Fe^{3+}/Fe^{2+} of amphibole in the sample (calculated from the average Fe^{3+}/Fe_{Total} determined from XAFS analyses and the average wt% FeO found from EPMA analysis) by the average $K^{Fe^{3+}/Fe^{2+}}$ for basalt determined from our experimental study. The Fe^{3+}/Fe^{2+} of the melt was translated to an oxygen fugacity relative to NNO using Equation 7 of Kress and Carmichael (1991) and the equation for fugacity at the NNO buffer from O'Neill and Powneeby (1993). The inputs to the equation were the sample's average Fe^{3+}/Fe^{2+}_{melt} (determined in the last step), whole rock Al_2O_3, FeO, CaO, Na_2O, and K_2O converted to mole fraction; a temperature of 1062 °C; and a pressure of 550 MPa. The temperature and pressure are the average temperature and pressure of amphibole crystallization reported by Goltz et al. (2020).

Calculated oxygen fugacity for our sample set has a considerable range, from NNO+1.9 to NNO+4 (Fig. 9; Table 5). This range overlaps with estimates of the oxygen fugacity of andesitic lavas that erupted in 2001 (NNO+1.5–2.1; Humphreys et al. 2006). The central assumption of the above calculation is that the Fe^{3+}/Fe_{Total} of amphibole is primitive and reflects the oxygen fugacity of equilibrium melts; it does not account for secondary

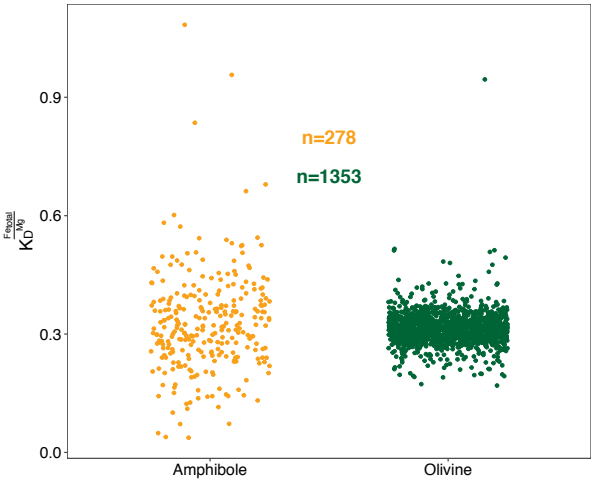

Figure 8. Fe_{Total}-Mg K_D of amphibole (orange) and olivine (green) reported from the LEPR database. Jitter has been introduced to the x-axis for clarity. The spread of amphibole K_D is much larger than that of olivine, though the mean value is similar. One potential explanation for the wider distribution of amphibole K_D is the inability to account for Fe^{3+} in amphibole, which would have a significant effect on the Fe^{3+}-bearing amphibole but would minimally affect olivine K_D. (Color online.)

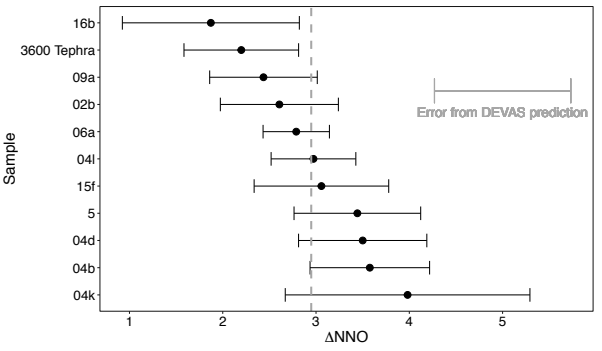

Figure 9. Calculated f_{O_2} by sample by increasing calculated oxygen fugacity. Error bars represent the propagated standard deviation of the average ferric-ferrous ratio for each sample. Gray error bar represents uncertainty in f_{O_2} calculation propagated from DEVAS predicted Fe^{3+}/Fe_{Total} (i.e., the minimum uncertainty). Dashed gray line represents average calculated f_{O_2}.

alteration of Fe^{3+} in amphibole, which will be thoroughly discussed in the following sections and which we will show is our preferred interpretation of the upper range of calculated oxygen fugacity. Two samples, amphibole-bearing cumulate 16B and the 3600 BP tephra have the lowest calculated f_{O_2} of our sample set and, on average, overlap with the estimates for oxygen fugacity from Humphreys et al. (2006). We interpret these samples as being reflective of the primitive f_{O_2} of magmas at Shiveluch, ~NNO+2. Samples with higher f_{O_2} (i.e., all analyzed mafic enclaves and amphibole-bearing cumulate 04L) may reflect actual variability in magmatic f_{O_2} caused by mantle source heterogeneity, differential slab fluid contribution, or crustal processes; the samples could also reflect secondary alteration/dehydrogenation of amphibole in the enclaves.

Calculated f_{O_2} is not reflective of real variability and changes in magmatic f_{O_2}

We first consider the notion that the range in calculated f_{O_2} in our sample set is reflective of real variability in magmatic f_{O_2} at Shiveluch. The potential contributions of mantle source heterogeneity, slab fluids, and crustal processes (i.e., fractional crystallization and crustal assimilation) are evaluated for these samples in the context of previously published geochemical and petrological measurements and observations of these samples [Goltz et al. (2020) for enclaves and cumulates and Ponomareva et al. (2007) and Volynets et al. (1997) for the tephra].

We use the V/Sc ratio of our samples to determine if mantle source heterogeneity in f_{O_2} may be responsible for the heterogeneity in our samples' calculated f_{O_2}. The vanadium to scandium ratio of primitive melts is strongly dependent on the oxygen fugacity of their mantle source because of the changes in the partitioning behavior of vanadium with oxygen fugacity due to changes in its valence state (e.g., Lee et al. 2005; Mallmann and O'Neill 2009). Assuming that the enclaves and tephra were generated through similar degrees of melting of mantle peridotite and that fractional crystallization did not significantly alter the samples' V/Sc, differences in V/Sc would be largely attributable to differences in source f_{O_2}. The enclaves and tephra have a smaller range in V/Sc (6.7–7.6) than would be expected from the wide

range of f_{O_2} calculated from the amphibole Fe^{3+}/Fe^{2+} (a range of >5 V/Sc; Lee et al. 2005), meaning that the samples in this study likely had similar primary f_{O_2} and that the observed range is not a function of mantle source f_{O_2} heterogeneity.

The Ba/Th ratio of our samples is used as a proxy to understand the influence of slab fluids on magmatic f_{O_2} in our samples. Fluids from mineral dehydration reactions in the downgoing slab contain solutes that are thought to be oxidants and have been used to explain the higher average f_{O_2} of arc magmas relative to mid-ocean ridge basalts (MORB; e.g., Parkinson and Arculus 1999; Kelley and Cottrell 2009; Brounce et al. 2014; Iacovino et al. 2020; Gaborieau et al. 2020), though the claim that fluids and their solutes are the cause of the higher than average magmatic f_{O_2} is debated (e.g., Carmichael 1991; Lee et al. 2005; Gaetani 2016). Barium—a large-ion lithophile and fluid-mobile element—is considered a proxy for fluid contribution from the downgoing slab. In the most general sense, the higher a melt's concentration of Ba, the higher its expected water content, although this generalization does not hold true when comparing variation in Ba and H_2O content in arc volcanoes worldwide (e.g., Plank et al. 2013) due to variability in the composition of certain downgoing sediments in which Ba is enriched (e.g., Plank and Langmuir 1998). To separate sediment and fluid signals, we use the ratio of barium to thorium, a relatively fluid-immobile element; this ratio has been used with success in the interpretation of fluid and sediment signals at other arcs (e.g., Patino et al. 2000). If variable melt water content caused the variability in calculated f_{O_2} in our samples, a positive correlation between Ba/Th and calculated f_{O_2} would be expected. Figure 10 shows that there is no correlation between Ba/Th and calculated f_{O_2}. The lack of correlation between Ba/Th and f_{O_2} suggests that melt water content cannot account for the observed range in f_{O_2}.

Crustal processes—including fractional crystallization, crustal assimilation, and magma mixing—are also thought to affect the f_{O_2} of melts at subduction settings. Fractional crystallization throughout the crustal column has been proposed to "auto-oxidize" primitive melts through the preferential fractionation of Fe^{2+} compared to Fe^{3+} (e.g., Ulmer et al. 2018; Tang et al. 2018). However, such auto-oxidative effects have not been observed in natural samples at arc settings (e.g., Kelley and Cottrell 2012; Brounce et al. 2014; Grocke et al. 2016). There is no correlation between whole rock differentiation indices (i.e., MgO and SiO_2) and calculated f_{O_2} in our sample set (Fig. 10). The lack of correlation between f_{O_2} and differentiation indices suggests that variability in calculated f_{O_2} in our sample set cannot be attributable to magmatic differentiation.

The presence of plagioclase xenocrysts in enclaves with higher calculated f_{O_2} and the lack thereof in samples with relatively low-calculated f_{O_2} may suggest that crustal assimilation increased magmatic f_{O_2}. Assimilation of oxidized crustal material has been suggested as a mechanism for the oxidation of melts throughout the crustal column (e.g., Ague and Brimhall 1988; Lee et al. 2005, 2012); however, a recent study of the oxidation state of evolved Central Andean magmas (known for their relatively high degree of crustal assimilation; e.g., Hildreth and Moorbath 1988) showed that crustal assimilation alone could not account for a >3 log unit range in f_{O_2} in those samples (Grocke et al. 2016).

Xenocrystic plagioclase in the enclaves at Shiveluch is evidence of contamination with more evolved material (either partially crystalline andesite or intermediate to felsic crust). On average, the enclaves have a higher calculated f_{O_2} than the cumulate sample 16B and the 3600 BP tephra, which lack evidence for extensive crustal assimilation (Volynets et al. 1997; Goltz et al. 2020). A calculation of the amount of magnetite needed in a crustal assimilant to oxidize the enclaves from ~NNO+2 (the average f_{O_2} preserved in amphibole in 16B and the 3600 BP tephra, inferred to be the primitive oxygen fugacity of magmas at Shiveluch) to their measured oxygen fugacity shows that crustal assimilation alone cannot account for the relatively high f_{O_2} calculated from amphiboles in the enclaves (see Online Materials[1]). In conclusion, the variable, high f_{O_2} calculated from amphibole in mafic enclaves in our sample set is not likely reflective of real variability in magmatic f_{O_2}. The f_{O_2} of primitive magmas at Shiveluch is interpreted to be equivalent to the lowest f_{O_2} samples, ~NNO+2. In the following section, we evaluate the possibility that the relatively high average Fe^{3+}/Fe_{Total} in the enclaves is reflective not of primitive magmatic f_{O_2} but of secondary alteration and hydrogen loss during residence in a hot zone in the shallow crust.

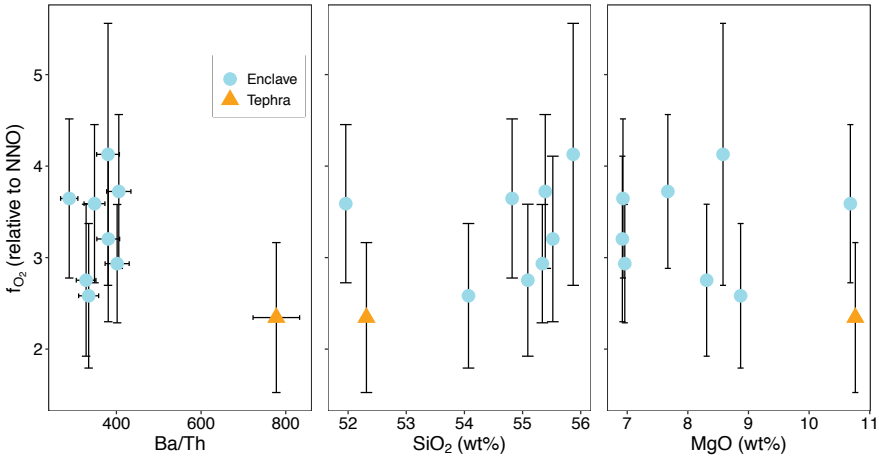

Figure 10. Calculated average f_{O_2} vs. whole rock Ba/Th, MgO, and SiO_2. Shape corresponds to sample classification (i.e., cumulate, enclave, or tephra). There is no correlation between any of these variables and the calculated f_{O_2}. (Color online.)

Tracking multiple episodes of mafic recharge using dehydrogenation of amphibole

Loss of hydrogen from amphibole is primarily accompanied by a corresponding increase in Fe^{3+} by the substitution:

$$OH^- + Fe^{2+} \leftrightarrow Fe^{3+} + O^{2-} + \tfrac{1}{2}H_2$$

(Dyar et al. 1993; Popp et al. 1995b). Amphibole dehydrogenation can occur as a result of re-equilibration with magmas at different pressures, temperatures, f_{O_2}, and/or f_{H_2} than the liquid with which the primary amphibole was in equilibrium (e.g., Dyar et al. 1993; Miyagi et al. 1998; King et al. 1999), and the rate of amphibole dehydrogenation is limited by the rate of diffusion of hydrogen through amphibole (Graham 1981; Graham et al. 1984). Dehydrogenation of amphibole in the enclaves could occur after the mafic liquids were quenched in the andesite host magma before eruption and would increase the amphibole Fe^{3+}/Fe_{Total}. Pre-eruptive amphibole dehydrogenation during sub-solidus ascent of mafic enclaves could explain the relatively high average amphibole Fe^{3+}/Fe_{Total} in the enclaves.

We model the loss of hydrogen from amphibole as a solid-state diffusive process. The assumption for our calculations is that dehydrogenation initiated when the mafic magmas were injected into the host andesite and quenched as enclaves. The relatively shallow depth and lower water content of the andesite relative to the mafic parents are conducive to amphibole dehydrogenation during sub-solidus ascent (e.g., King et al. 2018). The glassy, rapidly quenched texture of the enclaves, and the lack of breakdown rims around amphibole crystals imply that they were not slowly cooled below the amphibole-in curve (Humphreys et al. 2006; King et al. 2018; Goltz et al. 2020). In our calculation, we assume that the average amphibole in the enclaves initially had Fe^{3+}/Fe_{Total} equal to the average of amphibole in the most reduced sample, 16B (35.1%), and calculate the percent dehydrogenation required to oxidize amphibole from this starting condition to its average measured Fe^{3+}/Fe_{Total} (40.7–59.1%; Table 5). We calculate the amount of hydrogen in the un-dehydrogenated amphibole using the equation of King et al. (1999) and the Ti, Al^{VI}, and Fe^{3+} of the average amphibole in each sample on a 24 oxygen per formula unit basis, given a Fe^{3+}/Fe_{Total} equal to 35%. The moles of hydrogen lost (equal to the difference in moles of Fe^{3+} in the amphibole with $Fe^{3+}/Fe_{Total} = 35\%$ and with the average measured Fe^{3+}/Fe_{Total} in the sample) relative to the amount to the moles of hydrogen in the un-dehydrogenated amphibole is used as a target for forward modeling of hydrogen diffusion, thus allowing us to calculate the amount of time necessary between mafic magma injection and eruption to account for the average Fe^{3+}/Fe_{Total} of amphibole in each enclave, as described below. Percent dehydrogenation ranged from 6.5 to 25%, which corresponds to a 6 to 22% change in Fe^{3+}/Fe_{Total}. This difference in Fe^{3+}/Fe_{Total} is not detectible given the accuracy of our technique, and, as a consequence, observable zoning in Fe^{3+}/Fe_{Total} is not expected.

The average residence time of each enclave in the andesite host magma at Shiveluch is calculated by solving for time (t) in the approximate solution of the diffusion equation for an infinite cylinder with radius, a, and fractional loss, f (Crank 1975); this approximation is valid for values of f between 0–0.6 where 0 corresponds to zero hydrogen loss, and 1 would be complete hydrogen loss from amphibole:

$$f \cong \left(\frac{4}{\sqrt{\pi}}\right)\left(\frac{Dt}{a^2}\right)^{0.5} - \left(\frac{Dt}{a^2}\right) \quad (1)$$

where D is the diffusion coefficient for H in amphibole. Fractional loss, f, was equal to percent dehydrogenation (see the last paragraph) in our calculation. The reported time is the lower of the two roots of this quadratic equation. We used the solution for an infinite cylinder because it is a simple geometry that closely resembles the geometry of acicular amphibole crystals, which have one short and one long dimension in 2D space. Following the analogy between the infinite cylinder and acicular amphibole geometries, the radius a of the infinite cylinder is akin to the short dimension of the amphibole crystal. In our calculation, a was set equal to 417 μm; it was calculated by dividing the average long edge of acicular amphiboles with measured Fe^{3+}/Fe_{Total} (1100 μm) by the average aspect ratio of 58 large (i.e., "long edge" ≥ 1.5 mm) amphiboles measured in hand sample (on average, 2.64). The infinite cylinder geometry is an imperfect geometric analogy to amphibole, however, because there is diffusion at all interfaces in an amphibole crystal (i.e., it does not have an infinite dimension), the time calculated using the infinite cylinder model is likely an upper bound.

Another limitation of our calculation is that anisotropic diffusion is not considered, although a study of kaersutite crystals shows that hydrogen diffusion along the long amphibole c-axis is five times faster than along the short b-axis (Ingrin and Blanchard 2000). We use a diffusion coefficient, D, determined by Graham et al. (1984) for bulk diffusion of H through amphibole; the value is an average rate of diffusion for the crystal irrespective of crystallographic orientation and is appropriate for our modified 1D model. Graham et al. (1984) found an Arrhenius relationship between log D and reciprocal temperature for various compositions of amphibole modeled as infinite cylinders or half-sheets as linear. We use their equation of a line for hornblende #3224 modeled as an infinite cylinder:

$$\log D = -7.62 - 4.39\left(\frac{10^3}{T}\right) \quad (2)$$

where T is temperature in degrees Kelvin and D is in cm^2/s. For our model, the diffusivity was calculated with a temperature of 840 °C, which is the average temperature of the andesite host magma at Shiveluch determined by multiple geothermometers (Dirksen et al. 2006; Humphreys et al. 2006).

Uncertainty in time was quantified using a Monte Carlo approach, wherein t was calculated for each sample using 10 000 random, normally distributed points centered around the sample's mean amphibole major element composition from probe analyses and mean amphibole Fe^{3+}/Fe_{Total}, with a standard deviation equal to 2 times the standard error of those quantities. Among the 10 000 generated compositions, points with percent dehydrogenation less than 0 were excluded from the calculation of time. This filter impacted only two samples with relatively low average Fe^{3+}/Fe_{Total}, 09a and 02b; for these two samples, 124 and 18 points were excluded (i.e., the lowest 1.24% and 0.18% of values), respectively. The filtering of this relatively low percentage of points has a neg-

ligible impact on the final calculated time. Because Equation 2 is nonlinear in time, the distribution of calculated times is not symmetric, so we report the median and interquartile range (IQR) of times rather than the mean and standard deviation (Table 5; Figs. 11a and 11b).

Enclave residence time in the andesite host ranges from 6 days (sample 09a) to 3.4 months (sample 04k; Table 5; Fig. 11a). The range of residence times shows a history of pre-eruptive mafic recharge on the timescale of days to months, consistent with findings based on high-Mg olivine xenocrysts and plagioclase phenocrysts in the host andesite erupted in 2001 from Shiveluch (Dirksen et al. 2006; Humphreys et al. 2006). There are at minimum three resolvable pulses of mafic recharge in our data: one at 6–13 days before eruption, one at a month before eruption, and another 2–3 months before eruption. We determined the residence times for 8 samples and then compared each sample with each other, a total of 28 unique pairs (Online Materials[1] Fig. S1). The residence times for a pair of samples is distinguishable if the 95% confidence envelope of the difference in their median residence times did not overlap zero (Fig. 11c). To do so, we found the difference between the 10 000 residence times calculated for each of 28 pairs of samples and calculated the median difference and the 95% confidence interval with the minimum width in the distribution. Our results (Fig. 11c) show two groups of samples with indistinguishable residence times within 95% confidence: samples 04d, 04b, 04k, and 5 (red colors in Fig. 11) and samples 09a, 02b, and 06a (blue colors in Fig. 11). Sample 09a overlaps with sample 02b, but not sample 06a, meaning that, while the three samples had similar residence times in the host andesite, sample 09a may have been injected at a slightly earlier time. Sample 15f (yellow in Fig. 11a) overlaps with samples in neither group and was injected into the andesite at a time intermediate between the two groups. Overall, samples with similar residence times were likely injected into a hot, shallow andesite storage region at around the same time.

Mafic enclave samples with similar residence time but variable bulk rock differentiation indices (i.e., Mg#) indicate the existence

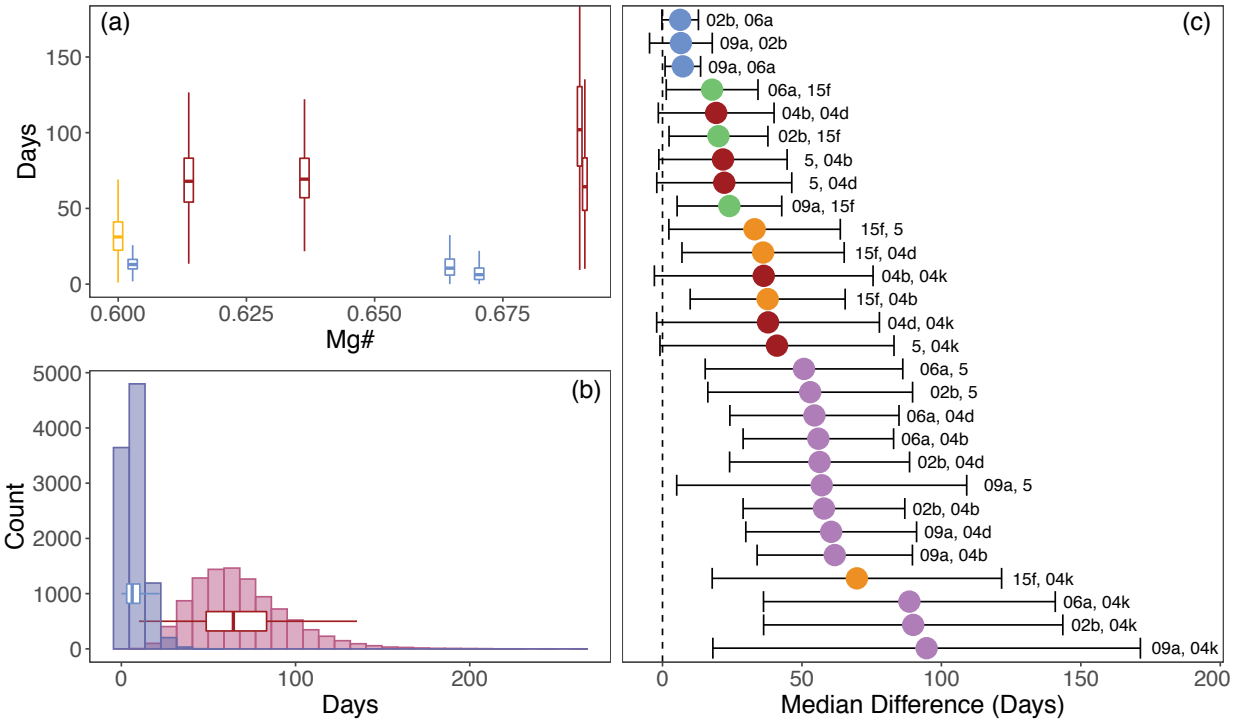

Figure 11. (**a**) Box-and-whisker plot showing median, interquartile range, and extremes of calculated residence time of each sample in an andesitic magma vs. sample Mg#. Boxes are centered on the Mg# of each sample, and the width the two more magnesian boxes is narrower because they overlap significantly in Mg#. Red samples have longer median residence times than samples colored blue. Sample 15f, which overlaps with neither group, is colored yellow. There is no correlation between sample Mg# and median residence time. (**b**) Histograms and box-and-whisker plots of calculated residence times for samples 05 (red) and 09a (blue) from Monte Carlo calculations showing how the distribution of points from the calculation translate to the box and whisker visual statistical summary. (**c**) Results of Monte Carlo calculation of 95% confidence interval (CI) and median difference between 28 pairs of samples. Uncertainty is calculated as CI/2. Sample pairs with uncertainty bars (i.e., the 95% confidence interval) overlapping zero (dashed line) have indistinguishable residence times in the host andesite within error. Color corresponds to the relative residence time of samples in the pair. Pairs where both samples have relatively short median residence times are colored blue, pairs where both samples have relatively long median residence times are colored red, pairs where one sample has a relatively short and one sample has a relatively long residence time are colored lilac, pairs with a sample with a short residence time and intermediate sample 15f are colored green, and pairs with a sample with a long residence time and intermediate sample 15f are colored yellow. From this analysis we are able to resolve a minimum of three pulses of magma recharge. We find that samples 09a, 06a, and 02b were injected into the host andesite within two weeks of the eruption and that this group of samples is distinguishable from samples 04b, 04d, 04k, and 5, which recharged the host andesite 2–3 months before eruption. Sample 15f was injected into the host andesite at 1 month before eruption, temporally between the two other groups. (Color online.)

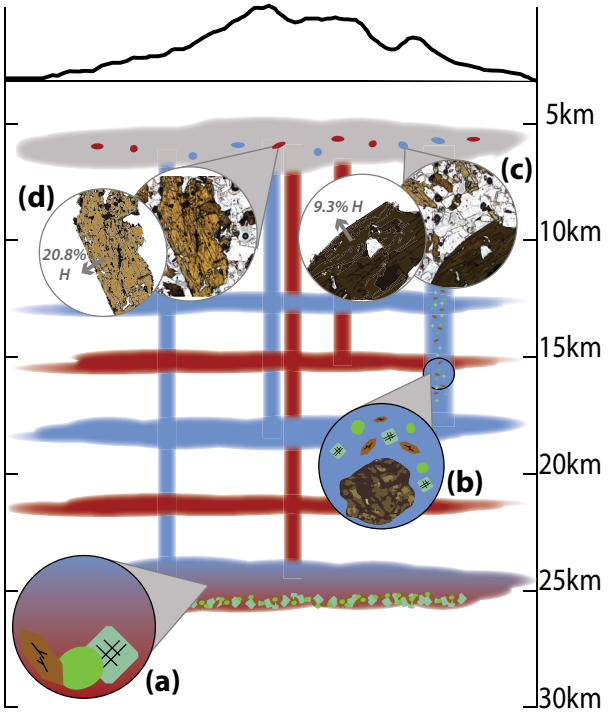

Figure 12. Schematic model for enclave formation and plumbing under Shiveluch over time based on amphibole Fe^{3+}/Fe_{Total}. Colors correspond to relative injection time as in Figure 11 (i.e., blue sills and enclaves are injected at later times than red sills and enclaves) except for the andesite, which is colored gray. From our data, we can resolve a minimum of three pulses of mafic recharge. Compositionally, the magmas injected during each recharge event were at different stages of differentiation and originated from different sills. Sills in this diagram are within the range of depths calculated for amphibole crystallization by Goltz et al. (2020); the maximum depth of the andesite is constrained by Dirksen et al. (2006). (**a**) A magnesian magma injected to the andesite at an earlier time (red) could be related to a later-injected, less magnesian magma (blue) by fractional crystallization of amphibole (brown), olivine (green), and clinopyroxene (light green) over time; fractional crystallization of these phases relates primitive magmas at this volcano to more evolved melts (Goltz et al. 2020). (**b**) Recharge magmas carry phenocrysts (phases as identified in **a**) and crustal cumulates to the shallow andesite. (**c** and **d**) Upon injection to the andesite, amphibole dehydrogenates; the extent of the dehydrogenation depends on the rate of diffusion of H through amphibole and the residence time of the crystal in the shallow andesite. (**c** and **d**) Plane-polarized light images of sample 06a (**c**) and 04d (**d**) and a vectorized rendering of an amphibole in those samples. The arrow represents dehydrogenation of the amphibole during its residence time; the percentage dehydrogenation for 06a is calculated to be 9.3% and is 20.8% for 04d. (Color online.)

of multiple mafic recharge bodies in the plumbing system under Shiveluch at various states of fractional crystallization evolution. There is no correlation between differentiation index and percent dehydrogenation (Fig. 11a) within these two groups of enclaves. This indicates that the recharge magmas injected into the andesite at a given time do not represent liquids evolving along a liquid line of descent of a single mafic recharge magma. To account for the distribution in magma composition at a given time of recharge, two to three distinct magma storage areas with variable Mg# must have recharged the andesitic magma over a small-time interval.

We interpret the enclaves to represent contributions from different mafic magma storage regions in the crust over time and identify a minimum of three distinct times when the andesite was recharged with at least two mafic recharge magmas (within two weeks of a month before and two to three months before the eruption) of differing compositions (Fig. 12). The mafic magma bodies may be related to a single parental magma in the deep crust that feeds multiple sills at shallower levels; this possibility requires evaluation in future studies.

Implications

In this study, we develop the Fe^{3+}/Fe^{2+} partitioning behavior between synthetic amphiboles and melt as an oxybarometer applicable to hydrous magmas at subduction settings and apply it to amphibole in mafic enclaves, cumulates, and tephra erupted from Shiveluch volcano in Kamchatka. This study proffers a single mineral-melt oxybarometer applicable to rocks with compositions ranging from basalt to dacite. We suggest that researchers seeking to apply our oxybarometer take care to analyze amphibole in rocks that are known to have been rapidly quenched upon eruption, which more reliably preserves magmatic f_{O_2} than amphibole in more slowly cooled rocks (King et al. 1999, 2018). For those who are looking to apply this oxybarometer to compositions intermediate, higher, or lower in NBO/T to the compositions in this study, we recommend applying the NBO/T-independent amphibole-melt Fe^{2+}/Mg partition coefficient as an oxybarometer using an estimate of melt Mg content.

For rocks where the magmatic oxygen fugacity is known independently, the partition coefficients determined in our study will also allow researchers to quantitatively determine the Fe^{3+}/Fe^{2+} of amphibole in their samples without direct measurement. This is a great improvement over the limited accuracy of Fe^{3+} determinations by site occupancy calculation from electron microprobe data. We also show the importance of explicitly considering Fe^{2+} in the calculation of a Fe-Mg distribution coefficient for amphibole; using Fe^{2+} as opposed to total iron in this situation leads to a much more consistent Fe-Mg distribution coefficient ($K^{Fe\text{-}Mg}$) for amphibole, which has proven to be a very useful petrological quantity for other Fe-Mg silicates. Finally, our analysis and diffusion modeling of amphibole in mafic enclaves has implications for temporal links between mafic recharge and eruption. Our results capture a prolonged period of pre-eruptive mafic recharge and show that each discernable mafic recharge event is not necessarily linked to an eruption at this volcano. Our finding extends the timeframe for pre-eruptive mafic recharge events inferred by other studies based on petrography, crystal chemistry, and modeling (e.g., Murphy et al. 2000; Browne et al. 2006; Ruprecht et al. 2008; Koleszar et al. 2012). The Fe^{3+} content of amphibole is thus a flexible tool that can be used to understand magmatic conditions and plumbing systems in greater detail.

Acknowledgments

The authors thank Tony Lanzirotti, Matt Newville, Ryan Tappero, and Sarah Nicholas for their help with the collection of XAFS data, and Cai Ytsma for her help with XAFS data processing. Paul Carpenter is thanked for help with and good humor during the collection of microprobe analyses. We also thank Helene Craigg and Kelsey Prissel for their help and support in the lab and during data collection at NSLS-II and APS. Noah McLean is also thanked for discussions on and help with statistical analysis of our data set. Penny King and an anonymous reviewer

are thanked for their constructive and considerate comments on an earlier draft of our manuscript, which indubitably improved its quality.

Funding

This research used Beamline 13-IDE of the Advanced Photon Source, a U.S. Department of Energy (DOE) Office of Science User Facility, operated for the DOE Office of Science by Argonne National Laboratory under Contract No. DE-AC02-06CH11357. This research also used the XFM Beamline of the National Synchrotron Light Source II, a U.S. Department of Energy (DOE) Office of Science User Facility operated for the DOE Office of Science by Brookhaven National Laboratory under Contract No. DE-SC0012704. The authors acknowledge support from Washington University in St. Louis for funding field and lab work associated with this project. A.E.G. acknowledges the McDonnell Center for the Space Sciences for funding. M.J.K. acknowledges support from National Science Foundation EAR Grant no. 1654683. M.C.M. and M.D.D. acknowledge funding from NASA grants NNX17AL07G and 80NSSC19K19K1008 and National Science Foundation EAR partner grants numbers 1754261 (MDD) and 1754268 (MCM). M.D.D., M.J.K., and M.C.M. also acknowledge support from National Science Foundation EAR partner grants numbers 20452 (M.D.D.), 204386 (M.J.K.), and 2042421 (M.C.M.).

References cited

Adam, J., Oberti, R., Cámara, F., and Green, T.H. (2007) An electron microprobe, LAM-ICP-MS and single-crystal X-ray structure refinement study of the effects of pressure, melt-H_2O concentration and f_{O_2} on experimentally produced basaltic amphiboles. European Journal of Mineralogy, 19, 641–655.

Ague, J.J., and Brimhall, G.H. (1988) Magmatic arc asymmetry and distribution of anomalous plutonic belts in the batholiths of California: Effects of assimilation, crustal thickness, and depth of crystallization. Geological Society of America Bulletin, 100, 912–927.

Alonso-Perez, R., Muntener, O., and Ulmer, P. (2008) Igneous garnet and amphibole fractionation in the roots of island arcs: experimental constraints on andesitic liquids. Contributions to Mineralogy and Petrology, 157, 541–558.

Aoki, K. (1963) The kaersutites and oxykaersutites from alkalic rocks of Japan and surrounding areas. Journal of Petrology, 4, 198–210.

Arculus, R.J., and Wills, K.J. (1980) The petrology of plutonic blocks and inclusions from the Lesser Antilles island arc. Journal of Petrology, 21, 743–799.

Armstrong, J.T., Donovan, J., and Carpenter, P. (2013) CALCZAF, TRYZAF and CITZAF: The use of multi-correction-algorithm programs for estimating uncertainties and improving quantitative X-ray analysis of difficult specimens. Microscopy and Microanalysis, 19, 812–813.

Ballhaus, C., Berry, R., and Green, D. (1990) Oxygen fugacity controls in the Earth's upper mantle. Nature, 348, 437–440.

Barclay, J., Rutherford, M.J., Carroll, M., Murphy, M., Devine, J., Gardner, J., and Sparks, R. (1998) Experimental phase equilibria constraints on pre-eruptive storage conditions of the Soufriere Hills magma. Geophysical Research Letters, 25, 3437–3440.

Beard, J.S. (1986) Characteristic mineralogy of arc-related cumulate gabbros: Implications for the tectonic setting of gabbroic plutons and for andesite genesis. Geology, 14, 848–851.

Bédard, J.H. (2010) Parameterization of the Fe/Mg exchange coefficient (Kd) between clinopyroxene and silicate melts. Chemical Geology, 274, 169–176.

Bindeman, I.N., Ponomareva, V.V., Bailey, J.C., and Valley, J.W. (2004) Volcanic arc of Kamchatka: a province with high-$\delta^{18}O$ magma sources and large-scale $^{18}O/^{16}O$ depletion of the upper crust. Geochimica et Cosmochimica Acta, 68, 841–865.

Blatter, D.L., and Carmichael, I.S.E. (2001) Hydrous phase equilibria of a Mexican high-silica andesite: A candidate for a mantle origin? Geochimica et Cosmochimica Acta, 65, 4043–4065.

Blatter, D.L., Sisson, T.W., and Hankins, B. (2017) Voluminous arc dacites as amphibole reaction-boundary liquids. Contributions to Mineralogy and Petrology, 172, 27.

Blundy, J., Melekhova, E., Ziberna, L., Humphreys, M.C.S., Cerantola, V., Brooker, R.A., McCammon, C.A., Pichavant, M., and Ulmer, P. (2020) Effect of redox on Fe-Mg-Mn exchange between olivine and melt and an oxybarometer for basalts. Contributions to Mineralogy and Petrology, 175, 1–32.

Boettcher, A., and O'Neil, J. (1980) Stable isotope, chemical, and petrographic studies of high-pressure amphiboles and micas: evidence for metasomatism in the mantle source regions of alkali basalts and kimberlites. American Journal of Science, 280, 594–621.

Botcharnikov, R.E., Koepke, J., Holtz, F., McCammon, C., and Wilke, M. (2005) The effect of water activity on the oxidation and structural state of Fe in a ferro-basaltic melt. Geochimica et Cosmochimica Acta, 69, 5071–5085.

Brounce, M., Kelley, K., and Cottrell, E. (2014) Variations in $Fe^{3+}/\Sigma Fe$ of Mariana Arc basalts and mantle wedge f_{O_2}. Journal of Petrology, 55, 2513–2536.

Browne, B.L., Eichelberger, J.C., Patino, L.C., Vogel, T.A., Dehn, J., Uto, K., and Hoshizumi, H. (2006) Generation of porphyritic and equigranular mafic enclaves during magma recharge events at Unzen Volcano, Japan. Journal of Petrology, 47, 301–328.

Bucholz, C.E., Gaetani, G.A., Behn, M.D., and Shimizu, N. (2013) Post-entrapment modification of volatiles and oxygen fugacity in olivine-hosted melt inclusions. Earth and Planetary Science Letters, 374, 145–155.

Buddington, A., and Lindsley, D. (1964) Iron-titanium oxide minerals and synthetic equivalents. Journal of Petrology, 5, 310–357.

Carey, C., Dyar, M., Boucher, T., and Giguere, S. (2017) Web-based software for preprocessing, matching, fitting, prediction, and visualization of spectroscopic data: the data exploration. Visualization, and Analysis of Spectra (DEVAS) Website, LPI, 1097.

Carmichael, I.S. (1991) The redox states of basic and silicic magmas: A reflection of their source regions? Contributions to Mineralogy and Petrology, 106, 129–141.

Coltorti, M., Bonadiman, C., Faccini, B., Gregoire, M., O'Reilly, S.Y., and Powell, W. (2007) Amphiboles from suprasubduction and intraplate lithospheric mantle. Lithos, 99, 68–84.

Core, D.P., Kesler, S.E., and Essene, E.J. (2006) Unusually Cu-rich magmas associated with giant porphyry copper deposits: Evidence from Bingham, Utah. Geology, 34, 41–44.

Cottrell, E., and Kelley, K.A. (2013) Redox heterogeneity in mid-ocean ridge basalts as a function of mantle source. Science, 340, 1314–1317.

Cottrell, E., Lanzirotti, A., Mysen, B., Birner, S., Kelley, K.A., Botcharnikov, R., Davis, F.A., and Newville, M. (2018) A Mössbauer-based XANES calibration for hydrous basalt glasses reveals radiation-induced oxidation of Fe. American Mineralogist, 103, 489–501.

Crank, J. (1975) The Mathematics of Diffusion, 421 p. Oxford University Press.

Dalpé, C., and Baker, D.R. (2000) Experimental investigation of large-ion-lithophile-element-, high-field-strength-element-and rare-earth-element-partitioning between calcic amphibole and basaltic melt: the effects of pressure and oxygen fugacity. Contributions to Mineralogy and Petrology, 140, 233–250.

Delaney, J., Bajt, S., Dyar, M., Sutton, S., McKay, G., and Roeder, P. (1996) Comparison of quantitative synchrotron microXANES (SmX) $Fe^{3+}/(Fe^{2+}+Fe^{3+})$ results for amphibole and silicate glass with independent measurements. Lunar and Planetary Science, 27, 299–300.

Dirksen, O., Humphreys, M.C.S., Pletchov, P., Melnik, O., Demyanchuk, Y., Sparks, R.S.J., and Mahony, S. (2006) The 2001–2004 dome-forming eruption of Shiveluch volcano, Kamchatka: Observation, petrological investigation and numerical modelling. Journal of Volcanology and Geothermal Research, 155, 201–226.

Donovan, J.J., and Tingle, T.N. (1996) An improved mean atomic number background correction for quantitative microanalysis. Microscopy and Microanalysis, 2, 1–7.

Donovan, J., Kremser, D., Fournelle, J., and Goemann, K. (2012) Probe for EPMA: Acquisition, automation and analysis. Probe Software, Inc.

Dyar, M.D., and Ytsma, C.Y. (2021) Effect of data set size on geochemical quantification accuracy with laser-induced breakdown spectroscopy. Spectrochimica Acta Part B: Atomic Spectroscopy, 177, 106073.

Dyar, M.D., McGuire, A.V., and Mackwell, S.J. (1992) Fe^{3+}/H^+ and D/H in kaersutites—Misleading indicators of mantle source fugacities. Geology, 20, 565–568.

Dyar, M.D., Mackwell, S.J., McGuire, A.V., Cross, L.R., and Robertson, J.D. (1993) Crystal chemistry of Fe^{3+} and H^+ in mantle kaersutite: Implications for mantle metasomatism. American Mineralogist, 78, 968–979.

Dyar, M.D., Breves, E.A., Gunter, M.E., Lanzirotti, A., Tucker, J.M., Carey, C.J., Peel, S.E., Brown, E.B., Oberti, R., Lerotic, M., and Delaney, J.S. (2016) Use of multivariate analysis for synchrotron micro-XANES analysis of iron valence state in amphiboles. American Mineralogist, 101, 1171–1189.

Gaborieau, M., Laubier, M., Bolfan-Casanova, N., Mccammon, C., Vantelon, D., Chumakov, A., Schiavi, F., Neuville, D., and Venugopal, S. (2020) Determination of $Fe^{3+}/\Sigma Fe$ of olivine-hosted melt inclusions using Mossbauer and XANES spectroscopy. Chemical Geology, 547, 119646

Gaetani, G.A. (2016) The behavior of $Fe^{3+}/\Sigma Fe$ during partial melting of spinel lherzolite. Geochimica et Cosmochimica Acta, 185, 64–77.

Gaillard, F., Scaillet, B., Pichavant, M., and Bény, J. (2001) The effect of water and f_{O_2} on the ferric-ferrous ratio of silicic melts. Chemical Geology, 174, 255–273.

Gavrilenko, M., Herzberg, C., Vidito, C., Carr, M.J., Tenner, T., and Ozerov, A. (2016) A calcium-in-olivine geohygrometer and its application to subduction zone magmatism. Journal of Petrology, 57, 1811–1832.

Gavrilenko, M., Krawczynski, M., Ruprecht, P., Li, W., and Catalano, J.G. (2019) The quench control of water estimates in convergent margin magmas. American Mineralogist, 104, 936–948.

Goltz, A.E., Krawczynski, M.J., Gavrilenko, M., Gorbach, N.V., and Ruprecht, P. (2020) Evidence for superhydrous primitive arc magmas from mafic enclaves at Shiveluch volcano, Kamchatka. Contributions to Mineralogy and Petrology, 175, 1–26.

Graham, C.M. (1981) Experimental hydrogen isotope studies III: Diffusion of hydrogen in hydrous minerals, and stable isotope exchange in metamorphic rocks. Contributions to Mineralogy and Petrology, 76, 216–228.

Graham, C.M., Harmon, R.S., and Sheppard, S.M. (1984) Experimental hydrogen isotope studies: Hydrogen isotope exchange between amphibole and water. American Mineralogist, 69, 128–138.

Greene, A.R., DeBari, S.M., Kelemen, P.B., Blusztajn, J., and Clift, P.D. (2006) A detailed geochemical study of island arc crust: The Talkeetna arc section,

south-central Alaska. Journal of Petrology, 47, 1051–1093.
Grocke, S.B., Cottrell, E., de Silva, S., and Kelley, K.A. (2016) The role of crustal and eruptive processes versus source variations in controlling the oxidation state of iron in Central Andean magmas. Earth and Planetary Science Letters, 440, 92–104.
Hamilton, D., Burnham, C.W., and Osborn, E. (1964) The solubility of water and effects of oxygen fugacity and water content on crystallization in mafic magmas. Journal of Petrology, 5, 21–39.
Hawthorne, F.C., and Oberti, R. (2007) Amphiboles: Crystal chemistry. Reviews in Mineralogy and Geochemistry, 67, 1–54.
Helz, R.T. (1973) Phase relations of basalts in their melting range at P_{H_2O} = 5 kb as a function of oxygen fugacity: Part I. Mafic phases. Journal of Petrology, 14, 249–302.
Hildreth, W., and Moorbath, S. (1988) Crustal contributions to arc magmatism in the Andes of central Chile. Contributions to Mineralogy and Petrology, 98, 455–489.
Hon, R., and Weill, D. (1982) Heat balance of basaltic intrusion vs granitic fusion in the lower crust. EOS, Trans AGU, 63, 470.
Hou, T., Botcharnikov, R., Moulas, E., Just, T., Berndt, J., Koepke, J., Zhang, Z., Wang, M., Yang, Z., and Holtz, F. (2020) Kinetics of Fe-Ti oxide re-equilibration in magmatic systems: Implications for thermo-oxybarometry. Journal of Petrology, 61, egaa116.
Humphreys, M.C., Blundy, J.D., and Sparks, R.S.J. (2006) Magma evolution and open-system processes at Shiveluch Volcano: Insights from phenocryst zoning. Journal of Petrology, 47, 2303–2334.
Iacovino, K., Guild, M.R., and Till, C.B. (2020) Aqueous fluids are effective oxidizing agents of the mantle in subduction zones. Contributions to Mineralogy & Petrology, 175.
Ingrin, J., and Blanchard, M. (2000) Hydrogen mobility in single crystal kaersutite. EMPG VIII. Journal of Conference Abstracts, 5:52.
Jagoutz, O., Müntener, O., Schmidt, M.W., and Burg, J. (2011) The roles of flux- and decompression melting and their respective fractionation lines for continental crust formation: Evidence from the Kohistan arc. Earth and Planetary Science Letters, 303, 25–36.
Jiang, G., Zhao, D., and Zhang, G. (2009) Seismic tomography of the Pacific slab edge under Kamchatka. Tectonophysics, 465, 190–203.
Kajfosz, J., and Kwiatek, W.M. (1987) Nonpolynomial approximation of background in X-ray spectra. Nuclear Instruments and Methods in Physics Research Section B: Beam Interactions with Materials and Atoms, 22, 78–81.
Kelley, K.A., and Cottrell, E. (2009) Water and the oxidation state of subduction zone magmas. Science, 325, 605–607.
——— (2012) The influence of magmatic differentiation on the oxidation state of Fe in a basaltic arc magma. Earth and Planetary Science Letters, 329-330, 109–121.
King, P., Hervig, R., Holloway, J., Vennemann, T., and Righter, K. (1999) Oxy-substitution and dehydrogenation in mantle-derived amphibole megacrysts. Geochimica et Cosmochimica Acta, 63, 3635–3651.
King, P., Hervig, R., Holloway, J., Delaney, J., and Dyar, M. (2000) Partitioning of Fe^{3+}/Fe_{Total} between amphibole and basanitic melt as a function of oxygen fugacity. Earth and Planetary Science Letters, 178, 97–112.
King, P.L., Wheeler, V.M., Renggli, C.J., Palm, A.B., Wilson, S.A., Harrison, A.L., Morgan, B., Nekvasil, H., Troitzsch, U., Mernagh, T., and others. (2018) Gas-solid reactions: Theory, experiments and case studies relevant to earth and planetary processes. Reviews in Mineralogy and Geochemistry, 84, 1–56.
Klein, M., Stosch, H., and Seck, H. (1997) Partitioning of high field-strength and rare-earth elements between amphibole and quartz-dioritic to tonalitic melts: an experimental study. Chemical Geology, 138, 257–271.
Koleszar, A.M., Kent, A.J., Wallace, P.J., and Scott, W.E. (2012) Controls on long-term low explosivity at andesitic arc volcanoes: Insights from Mount Hood, Oregon. Journal of Volcanology and Geothermal Research, 219-220, 1–14.
Krawczynski, M., and Olive, J. (2011) A new fitting algorithm for petrological mass-balance problems. AGUFM, 201153B-2613.
Krawczynski, M.J., Grove, T.L., and Behrens, H. (2012) Amphibole stability in primitive arc magmas: Effects of temperature, H_2O content, and oxygen fugacity. Contributions to Mineralogy and Petrology, 164, 317–339.
Kress, V.C., and Carmichael, I.S. (1991) The compressibility of silicate liquids containing Fe_2O_3 and the effect of composition, temperature, oxygen fugacity and pressure on their redox states. Contributions to Mineralogy and Petrology, 108, 82–92.
Kushiro, I., and Mysen, B.O. (2002) A possible effect of melt structure on the $Mg\text{-}Fe^{2+}$ partitioning between olivine and melt. Geochimica et Cosmochimica Acta, 66, 2267–2272.
Leake, B.E., Woolley, A.R., Arps, C.E.S., Birch, W.D., Gilbert, M.C., Grice, J.D., Hawthorne, F.C., Kato, A., Kisch, H.J., Krivovichev, V.G., and others. (1997) Nomenclature of amphiboles; report of the Subcommittee on Amphiboles of the International Mineralogical Association Commission on new minerals and mineral names. Mineralogical Magazine, 61, 295–310.
Leake, B.E., Woolley, A.R., Birch, W.D., Burke, E.A.J., Ferraris, G., Grice, J.D., Hawthorne, F.C., Kisch, H.J., Krivovichev, V.G., Schumacher, J.C., and others. (2003) Nomenclature of amphiboles: additions and revisions to the International Mineralogical Association's 1997 recommendations. Canadian Mineralogist, 41, 1355–1362.
Lee, C.T.A., Leeman, W.P., Canil, D., and Li, Z.A. (2005) Similar V/Sc systematics in MORB and arc basalts: implications for the oxygen fugacities of their mantle source regions. Journal of Petrology, 46, 2313–2336.
Lee, C.T.A., Luffi, P., Chin, E.J., Bouchet, R., Dasgupta, R., Morton, D.M., Le Roux, V., Yin, Q., and Jin, D. (2012) Copper systematics in arc magmas and implications for crust-mantle differentiation. Science, 336, 64–68.
Levin, V., Shapiro, N., Park, J., and Ritzwoller, M. (2002) Seismic evidence for catastrophic slab loss beneath Kamchatka. Nature, 418, 763–767.
Mallmann, G., and O'Neill, H.St.C. (2009) The crystal/melt partitioning of V during mantle melting as a function of oxygen fugacity compared with some other elements (Al, P, Ca, Sc, Ti, Cr, Fe, Ga, Y, Zr and Nb). Journal of Petrology, 50, 1765–1794.
Martin, R.F. (2007) Amphiboles in the igneous environment. Reviews in Mineralogy and Geochemistry, 67, 323–358.
Mathez, E. (1984) Influence of degassing on oxidation states of basaltic magmas. Nature, 310, 371–375.
McCanta, M.C., Rutherford, M.C., and Hammer, J.E. (2007) Pre-eruptive and syn-eruptive conditions in the Black Butte, California dacite: Insight into crystallization kinetics in a silicic magma system. Journal of Volcanology and Geothermal Research, 160, 263–284.
McGill, R., Tukey, J.W., and Larsen, W.A. (1978) Variations of box plots. The American Statistician, 32, 12–16.
Melekhova, E., Annen, C., and Blundy, J. (2013) Compositional gaps in igneous rock suites controlled by magma system heat and water content. Nature Geoscience, 6, 385–390.
Miyagi, I., Matsubaya, O., and Nakashima, S. (1998) Change in D/H ratio, water content and color during dehydration of hornblende. Geochemical Journal, 32, 33–48.
Moore, G., Righter, K., and Carmichael, I. (1995) The effect of dissolved water on the oxidation state of iron in natural silicate liquids. Contributions to Mineralogy and Petrology, 120, 170–179.
Mungall, J.E. (2002) Roasting the mantle: Slab melting and the genesis of major Au and Au-rich Cu deposits. Geology, 30, 915–918.
Murphy, M.D., Sparks, R.S.J., Barclay, J., Carroll, M.R., and Brewer, T.S. (2000) Remobilization of andesite magma by intrustion of mafic magma at the Soufriere Hills Volcano, Montserrat, West Indies. Journal of Petrology, 41, 21–42.
Mysen, B.O. (1988) Structure and Properties of Silicate Melts, Vol. 4, 354 p. Elsevier.
Nikulin, A., Levin, V., Shuler, A., and West, M. (2010) Anomalous seismic structure beneath the Klyuchevskoy Group, Kamchatka. Geophysical Research Letters, 37.
Nikulin, A., Levin, V., Carr, M., Herzberg, C., and West, M. (2012) Evidence for two upper mantle sources driving volcanism in Central Kamchatka. Earth and Planetary Science Letters, 321-322, 14–19.
Nishizawa, T., Nakamura, H., Churikova, T., Gordeychik, B., Ishizuka, O., Haraguchi, S., Miyazaki, T., Vaglarov, B.S., Chang, Q., Hamada, M., and others. (2017) Genesis of ultra-high-Ni olivine in high-Mg andesite lava triggered by seamount subduction. Scientific Reports, 7, 1–11.
Oberti, R., Hawthorne, F.C., Cannillo, E., and Cámara, F. (2007) Long-range order in amphiboles. Reviews in Mineralogy and Geochemistry, 67, 125–171.
O'Neill, H.St.C., and Nell, J. (1997) Gibbs free energies of formation of RuO_2, IrO_2, and OsO_2: A high-temperature electrochemical and calorimetric study. Geochimica et Cosmochimica Acta, 61, 5279–5293.
O'Neill, H.St.C., and Pownceby, M.I. (1993) Thermodynamic data from redox reactions at high temperatures. I. An experimental and theoretical assessment of the electrochemical method using stabilized zirconia electrolytes, with revised values for the Fe-"FeO", Co-CoO, Ni-NiO and $Cu\text{-}Cu_2O$ oxygen buffers, and new data for the $W\text{-}WO_2$ buffer. Contributions to Mineralogy and Petrology, 114, 296–314.
Osborn, E.F. (1959) Role of oxygen pressure in the crystallization and differentiation of basaltic magma. American Journal of Science, 257, 609–647.
Papale, P., Moretti, R., and Barbato, D. (2006) The compositional dependence of the saturation surface of H_2O+CO_2 fluids in silicate melts. Chemical Geology, 229, 78–95.
Park, J., Levin, V., Brandon, M., Lees, J., Peyton, V., Gordeev, E., and Ozerov, A. (2002) A dangling slab, amplified arc volcanism, mantle flow and seismic anisotropy in the Kamchatka Plate Corner. In S. Stein and J.T. Freymueller, Eds., Plate Boundary Zones, p. 295–324. AGU.
Parkinson, I.J., and Arculus, R.J. (1999) The redox state of subduction zones: insights from arc-peridotites. Chemical Geology, 160, 409–423.
Parlak, O., Höck, V., and Delaloye, M. (2000) Suprasubduction zone origin of the Pozanti-Karsanti ophiolite (southern Turkey) deduced from whole-rock and mineral chemistry of the gabbroic cumulates. Geological Society, London, Special Publications, 173, 219–234.
Patino, L.C., Carr, M.J., and Feigenson, M.D. (2000) Local and regional variations in Central American arc lavas controlled by variations in subducted sediment

input. Contributions to Mineralogy and Petrology, 138, 265–283.
Peyton, V., Levin, V., Park, J., Brandon, M., Lees, J., Gordeev, E., and Ozerov, A. (2001) Mantle flow at a slab edge: Seismic anisotropy in the Kamchatka region. Geophysical Research Letters, 28, 379–382.
Phillips, M.W., Popp, R.K., and Clowe, C.A. (1988) Structural adjustments accompanying oxidation-dehydrogenation in amphiboles. American Mineralogist, 73, 500–506.
Plank, T., and Langmuir, C.H. (1998) The chemical composition of subducting sediment and its consequences for the crust and mantle. Chemical Geology, 145, 325–394.
Plank, T., Kelley, K.A., Zimmer, M.M., Hauri, E.H., and Wallace, P.J. (2013) Why do mafic arc magmas contain ~4 wt% water on average? Earth and Planetary Science Letters, 364, 168–179.
Ponomareva, V., Kyle, P., Pevzner, M., Sulerzhitsky, L., and Hartman, M. (2007) Holocene Eruptive History of Shiveluch Volcano, Kamchatka Peninsula, Russia. In J.C. Eichelberger, E. Gordeev, P.E. Izbekov, M. Kasahara, and J. Lees, Eds., Volcanism and Subduction: The Kamchatka Region, p. 263–282. American Geophysical Union.
Popp, R.K., Virgo, D., Yoder, H.S., Hoering, T.C., and Phillips, M.W. (1995a) An experimental study of phase equilibria and Fe oxy-component in kaersutitic amphibole: Implications for the f_{H_2} and a_{H_2O} in the upper mantle. American Mineralogist, 80, 534–548.
Popp, R.K., Virgo, D., and Phillips, M.W. (1995b) H deficiency in kaersutitic amphiboles: Experimental verification. American Mineralogist, 80, 1347–1350.
Putirka, K.D. (2008) Thermometers and barometers for volcanic systems. Reviews in Mineralogy and Geochemistry, 69, 61–120.
——— (2016) Amphibole thermometers and barometers for igneous systems and some implications for eruption mechanisms of felsic magmas at arc volcanoes. American Mineralogist, 101, 841–858.
Richards, J.P. (2011) High Sr/Y arc magmas and porphyry Cu±Mo±Au deposits: Just add water. Economic Geology, 106, 1075–1081.
Rowe, M.C., Kent, A.J., and Nielsen, R.L. (2009) Subduction influence on oxygen fugacity and trace and volatile elements in basalts across the Cascade Volcanic Arc. Journal of Petrology, 50, 61–91.
Ruprecht, P., Bergantz, G.W., and Dufek, J. (2008) Modeling of gas-driven magmatic overturn: Tracking of phenocryst dispersal and gathering during magma mixing. Geochemistry, Geophysics, Geosystems, 9.
Sisson, T., and Grove, T. (1993) Experimental investigations of the role of H_2O in calc-alkaline differentiation and subduction zone magmatism. Contributions to Mineralogy and Petrology, 113, 143–166.
Sugawara, T. (2001) Ferric iron partitioning between plagioclase and silicate liquid: Thermodynamics and petrological applications. Contributions to Mineralogy and Petrology, 141, 659–686.
Sun, W-D., Liang, H-y., Ling, M-X., Zhan, M-Z., Ding, X., Zhang, H., Yang, X-y., Li, Y-L., Ireland, T.R., Wei, Q-R., and Fan, W-M. (2013) The link between reduced porphyry copper deposits and oxidized magmas. Geochimica et Cosmochimica Acta, 103, 263–275.
Tang, M., Erdman, M., Eldridge, G., and Lee, C.A. (2018) The redox "filter" beneath magmatic orogens and the formation of continental crust. Science Advances, 4.
Tiepolo, M., Oberti, R., Zanetti, A., Vannucci, R., and Foley, S.F. (2007) Trace-element partitioning between amphibole and silicate melt. Reviews in Mineralogy and Geochemistry, 67, 417–452.
Toplis, M.J., and Corgne, A. (2002) An experimental study of element partitioning between magnetite, clinopyroxene and iron-bearing silicate liquids with particular emphasis on vanadium. Contributions to Mineralogy and Petrology, 144, 22–37.
Ulmer, P., Kaegi, R., and Müntener, O. (2018) Experimentally derived intermediate to silica-rich arc magmas by fractional and equilibrium crystallization at 1.0 GPa: An evaluation of phase relationships, compositions, liquid lines of descent and oxygen fugacity. Journal of Petrology, 59, 11–58.
Ungaretti, L. (1980) Recent developments in X-ray single crystal diffractometry applied to the crystal-chemical study of amphiboles. Godisnjak Jugoslavenskog Centra za Kristalografiju, 15, 29–65.
Volynets, O., Ponomareva, V., and Babansky, A. (1997) Magnesian basalts of Shiveluch andesite volcano. Kamchatka. Petrology, 5, 206–221.
Wilke, M., Behrens, H., Burkhard, D.J., and Rossano, S. (2002) The oxidation state of iron in silicic melt at 500 MPa water pressure. Chemical Geology, 189, 55–67.
Yogodzinski, G., Lees, J., Churikova, T., Dorendorf, F., Wöerner, G., and Volynets, O. (2001) Geochemical evidence for the melting of subducting oceanic lithosphere at plate edges. Nature, 409, 500–504.
Zhang, H., Hirschmann, M., Cottrell, E., Newville, M., and Lanzirotti, A. (2016) Structural environment of iron and accurate determination of $Fe^{3+}/\Sigma Fe$ ratios in andesitic glasses by XANES and Mossbauer spectroscopy. Chemical Geology, 428, 48–58.
Zhang, H.L., Cottrell, E., Solheid, P.A., Kelley, K.A., and Hirschmann, M.M. (2018) Determination of $Fe^{3+}/\Sigma Fe$ of XANES basaltic glass standards by Mossbauer spectroscopy and its application to the oxidation state of iron in MORB. Chemical Geology, 479, 166–175.

Manuscript received February 24, 2021
Manuscript accepted October 27, 2021
Manuscript handled by Julie Roberge

Endnote:

[1]Deposit item AM-22-118031, Online Materials. Deposit items are free to all readers and found on the MSA website, via the specific issue's Table of Contents (go to http://www.minsocam.org/MSA/AmMin/TOC/2022/Nov2022_data/Nov2022_data.html).